JOURNAL OF COMPUTATIONAL PHYSICS 71, 429–473 (1987)

An Electromagnetic Field Algorithm for 2D Implicit Plasma Simulation*

RODNEY J. MASON

Los Alamos National Laboratory, Los Alamos, New Mexico 87545

Received May 23, 1986; revised October 6, 1986

A new, robust algorithm is presented for the implicit calculation of the electromagnetic fields used in the full-particle and hybrid modeling of 2D simulation plasmas. The algorithm allows for calculations at time steps Δt well in excess of the plasma period and for mesh scales Δx far exceeding the Debye length—with electron inertial terms retained. The implicit fields suppress the numerical instability associated with plasma waves. Still, the Δt remain constrained by an electron Courant limit. The algorithm is considerably simpler than earlier implicit schemes, and more complete in its treatment of field errors In its present form the algorithm is limited to plasmas moving and accelerating in a plane across a *single* component of magnetic field. An extension to include all the field components is suggested, however. In accordance with the *implicit moment method*, estimated electric and magnetic fields are obtained by solving Maxwell's equations self-consistently for a set of implicit sources, estimated with the aid of an auxiliary set of lower fluid moment equations (for component fluxes and density). The fluid pressure terms are treated explicitly, and the spatial differencing of the auxiliary moments is centered to facilitate the solution of the resultant field equations Solution for the single magnetic field component is obtained by one elliptic equation inversion, readily managed by a vectorized solver package. A subsequent irrotational old E-field correction is found to be crucial for the maintainence of anticipated quasi-neutrality. A concomitant rotational correction is needed for physical solutions in steep density gradient problems. We show that both corrections can be obtained simultaneously by referencing the deviations between the true currents flowing, and the currents predicted to flow in the plasma at the end of a cycle. The current correction is shown to be equivalent to the first (and usually sufficient) step of an iterative procedure leading to an exact solution for the fields In addition, we demonstrate that electrostatic solutions can be obtained from the implicit algorithm by setting the speed of light to very large multiples of its physical value. Comparisons are made with earlier moment and direct method approaches, and the scheme is related to previous classical hybrid models. Demonstrative applications are discussed.

1. INTRODUCTION

In particle-in-cell (PIC) plasma simulation [1, 2] a large number of particles, each representing many electrons or ions, are advanced in accordance with Newton's laws through electromagnetic fields determined from Maxwell's equations. In

0021-9991/87 $3.00

related hybrid schemes [3] a portion of the plasma electrons or ions are treated as fluids. The older full-particle explicit plasma simulation models [4] were limited to time steps less than a plasma period, i.e., $\omega_p \Delta t < 2$. With the invention of implicit plasma simulation schemes, this restraint was removed, first in one dimension [3, 5–15], and then in two-dimensions [16–20]—offering great promise for diverse applications. Yet, to date, 2D usage [21–24] has not been widespread, due, in part, to the complexity and sensitivity of the algorithms first proposed. This has encouraged the development of the new algorithm detailed here, which appears to be both simpler and more robust than the earlier approaches. The new algorithm is embodied in the 2D implicit hybrid simulation code ANTHEM.

Presently, ANTHEM is limited to plasmas moving in a plane through, say, E_x and E_y electric fields, and across a single mutually perpendicular B_z component of magnetic field. An extension of the algorithm to include all the remaining field components is, however, discussed. We use the moment method [9, 12, 16], solving Maxwell's equations for time-advanced sources predicted with a set of auxiliary fluid moment equations. With *explicit* pressures employed in these auxiliary equations, the predicted currents become simple algebraic functions of the *local* E-fields. In turn, through Ampere's law these E-fields become algebraic functions of $\nabla \times \mathbf{B}$. Substitution of these $\mathbf{E}$ expressions into Faraday's law leads, for the plasma flows considered, to a single elliptic equation for B_z. This is readily inverted with vectorized solver packages. Earlier approaches differ by treating either the static and/or dynamic pressure implicitly and by working iteratively with the scalar and vector electromagnetic potentials [16], or by using the direct implicit method, which leads to currents dependent on spatial derivatives of the E-field components [20]. Both prescriptions generate a much more complex set of field equations than those encountered in ANTHEM. A current-related rule is used in the new algorithm for the iterative correction of the fields to their exact values. The earlier methods have relied on only ad hoc corrections to the irrotational sub-portions of the E-fields. ANTHEM allows for the hybrid fluid modeling of selected components of the plasma. The former treatments have been confined to a PIC representation for all the electrons and ions.

We review the general features of the implicit moment method in the next section. Then, two modes of the ANTHEM field algorithm are spelled out in Section 3 (a preliminary outline has been given elsewhere [25–27]), and a full-field extension of the algorithm is suggested. Section 4 shows how the plasma coordinates are advanced in the implicit fields derived from the new algorithm. Section 5 discusses approximate correction of the fields. An Appendix discusses more complete iterative corrections. In Section 6 we summarize the operations performed in a typical ANTHEM cycle. The remaining sections provide additional background material. In Section 7 we show that electrostatic solutions can be obtained by artificially setting the speed of light to very large values. Section 8 compares our algorithm to approaches taken by other workers. Next, Section 9 discusses the existing hybrid implementation of the algorithm and speculates on future possibilities. The remaining Sections provide demonstrative applications, and our conclusions.

2. The Implicit Moment Method

Linear analysis shows [9, 11] that simulation can avoid the numerical instabilities related to the plasma waves, if the plasma coordinates are updated in *time-advanced* electric fields. At first, it might seem that knowledge of these fields would require the inversion of a very large matrix corresponding to the field and plasma equations. With 100 particles/cell this could amount to some 500 equations/cell, for example, so that for a 50×50 mesh one would need to invert more than 10^6 equations (which would, in turn, lead to the inversion of $10^6 \times 10^6$ size matrices!). This inversion problem is, however, markedly reduced in the moment method—simply by solving Maxwell's equations jointly with a set of auxiliary fluid equations (at least a set of momentum equations, possibly also a continuity equation). This procedure produces an implicitly *predicted* set of fields and sources to Maxwell's equations. The particles and any true fluids are then advanced in these predicted fields. Deviations between the predicted sources (i.e., currents) for Maxwell's equations, and those actually achieved are collected. These are used as sources through the moment equations for subsequent improvements to the fields, prior to a an update of the plasma coordinates to improved values, giving improved sources. This whole process can be iterated repeatedly, although a single correction—usually delayed to the beginning of the next cycle—has been found, in general, to suffice.

When the plasma is modeled at least partially with fluid components, these are advanced in time by a set of "true fluid equations." Analytically, the true fluid equations are identical in their lower moments to the auxiliary moment equations used for the fields. But in ANTHEM the true equations extend beyond continuity and momentum to include an energy (or entropy) equation, and a prescription for the heat flux. Numerically, the auxiliary lower moments, and the true fluid lower moments differ in ANTHEM because centered spatial differencing is generally used in the auxiliary equations, while Van Leer [28] spatial differencing is employed for the true fluids. An improved spatial treatment is needed for the true hydrodynamic advance to minimize numerical diffusion. However, it is skipped in the auxiliary equations governing fields to simplify, and to avoid mandatory iteration. The Van Leer differencing requires prior knowledge of the fluid velocities, which are known, only after the field and Maxwell sources have been derived, i.e., after the field equations have been solved.

a. How Implicit?

One is, of course, free to choose a degree of implicitness that suffices for the problems of interest—as a compromise between the utility and simplicity of the numerical scheme which results. When the sources to Maxwell's equations are left explicit, but the $\nabla \times \mathbf{B}$ of Ampere's law, and the $\nabla \times \mathbf{E}$ of Faraday's law are made implicit, one can use a time step Δt exceeding the Courant condition based on the speed of light, in performing electromagnetic simulations. Godfrey [29] showed this some years ago. Accordingly, uncoupled elliptic (Poisson) equations must be solved

separately for the B-field components, and the simplest option to use a leap-frog update of the fields [30] is lost.

Beyond this, to avoid the time step limitation from plasma oscillations which restrains calculations to $\omega_p \Delta t < 2$, one must make the E-field implicit in the differenced auxiliary momentum (i.e., current) equations [9, 13]. The elliptic field equations become inhomogeneous by this addition, and a symmetric matrix equation solver is needed for their inversion. Significant utility may be achieved for particle schemes at this stage, since with $\omega_p \Delta t \gg 1$ the use of time steps approaching the electron Courant limit, i.e., $0.1 < v_e \Delta t/\Delta x < 1.0$ with $\omega_p \Delta t > 1$, supresses the finite grid instability [16, 17]. (One reason for the development of a fluid capability in ANTHEM is that in very cold regions, where this Courant requirement cannot be satisfied, the use of fluid electrons can bypass this instability.)

Next, should one desire to describe plasmas in intense magnetic fields with the time step exceeding the electron cyclotron time, i.e., $\omega_c \Delta t > 1$, then the *velocity* must be implicit in the $\mathbf{v} \times \mathbf{B}$ terms of the component momentum equations which yield the new currents. With velocity implicit wherever $\mathbf{v} \times \mathbf{B}$ appears, the resultant elliptic equations are, in general, strongly coupled and nonsymmetric with stencils exceeding 9-points. But, for the simple case of motion, acceleration and E-fields in a plane perpendicular to a single component of $\mathbf{B}$, the system can be reduced to a single nonsymmetric 9-point elliptic equation for, say, B_z. This is the first operational mode available with ANTHEM. Less obviously, we have found that if $\mathbf{v}$ is left explicit in the elliptic equations for $\mathbf{B}$, but implicit in the current update, the resultant equations are largely decoupled with symmetric matrices, and stable—even when $\omega_c \Delta t \gg 1$. This second mode is available in ANTHEM, but still under evaluation, due to its unusual structure.

Finally, for the ability to use the implicit differencing scheme at time steps exceeding the Courant limit, i.e., $\Delta t > \Delta x/a_e$, where a_e is thermal speed of the fastest electrons, one must employ an implicit pressure [9, 16] or extrapolate the moment [17] equations. Freedom from an electron Courant limit can be useful, if variable cell sizes are desired—with very fine cells placed in inactive regions of a problem, where accuracy may not be too crucial. However, the use of either implicit pressure or extrapolation widely expands the stencil for the field solution matrix—presenting a special challange for inversion. For simplicity, therefore, we bypass extrapolation and retain explicit pressures in ANTHEM.

We now detail the field solution procedures employed.

3. The Field Prediction

For implicit fields we require a time-advanced current source in Ampere's law

$$\frac{\partial \mathbf{E}}{\partial t} = -4\pi \sum q_\alpha \mathbf{j}_\alpha + c\nabla \times \mathbf{B}, \tag{1}$$

which is solved with Faraday's law

$$\frac{\partial \mathbf{B}}{\partial t} = -c\nabla \times \mathbf{E} \tag{2}$$

to obtain the new E- and B-fields. Here and subsequently, $\sum$ is over the components α.

The $J_\alpha \equiv n_\alpha \mathbf{v}_\alpha$ terms in Eq. (1) are component fluxes, with n_α the component density and $\mathbf{v}_\alpha$ its velocity. The charges q_h and q_c are $-e$ for, say, hot and cold electron components in a laser-driven transport problem [3], while $q_i = +Ze$ for the ions. The $\nabla \cdot \mathbf{B} = 0$ Maxwell Equation reduces to $\partial B_z/\partial z = 0$, when only the single B_z component is allowed. Finally, the accumulated charge will give rise to E-fields obeying Gauss's equation

$$\nabla \cdot \mathbf{E} = 4\pi \sum q_\alpha n_\alpha. \tag{3a}$$

The E-field is related to the scalar electrostatic potential ϕ by the expression

$$\mathbf{E} = -\nabla\phi - \frac{1}{c}\frac{\partial \mathbf{A}}{\partial t}. \tag{3b}$$

Here, $\mathbf{A}$ is the magnetic vector potential, satisfying

$$\mathbf{B} = \nabla \times \mathbf{A}. \tag{3c}$$

The scalar potential is used principally as a diagnostic in our new algorithm, although it features in our Section 5 discussion of field corrections. Brackbill, Forslund, and Wallace [16–18] have used the vector potentials $\mathbf{A}$ as an intermediary in obtaining implicit $\mathbf{E}$ and $\mathbf{B}$ fields. We work with the fields directly. Time integrating Eq. (1), we obtain

$$\mathbf{E}^{(m+1)} = \mathbf{E}^{(m)} - 4\pi \sum q_\alpha \mathbf{j}_\alpha^{(*)} \Delta t + c\nabla \times \mathbf{B}^{(\dagger)} \Delta t. \tag{4}$$

We store all physical properties at time level-(m). Appropriate time averages are taken to form optimal centerings [3] at the time levels $(*)$ and $(^\dagger)$. Generally, the fully forward values $(*) = (^\dagger) = (m+1)$ give the most stable numerical results, while a choice slightly forward of center, e.g. $(m+0.55)$, gives stable results with improved accuracy. Denavit [13] and Langdon *et al.* [15] recommend a diversity of alternate centering prescriptions with improved damping characteristics for unwanted high frequency disturbances. To simplify the presentation we will generally invoke the fully forward time-centering choice in the discussion that follows.

Following the *moment method*, we calculate $\mathbf{j}^{(*)}$ by time-integrating a set *auxiliary momentum equations*

$$\frac{\partial \mathbf{j}_\alpha}{\partial t} = -\frac{\nabla \cdot \bar{\mathbf{P}}_\alpha}{m_\alpha} + \frac{n_\alpha q_\alpha}{m_\alpha}\left(\mathbf{E} + \frac{\mathbf{v}_\alpha \times \mathbf{B}}{c}\right). \tag{5}$$

Here, the pressure tensor $\bar{\mathbf{P}}_\alpha \equiv P_{\alpha\beta\gamma} \equiv m_\alpha n_\alpha v_\beta v_\gamma + (P_\alpha + P_{a\alpha\beta})\,\delta_{\beta\gamma}$, in which $\delta_{\beta\gamma}$ is the Kronecker delta, $P_\alpha \equiv n_\alpha \kappa T_\alpha$ is the scalar pressure, assuming isotropy of the random part of the component distributions [31], and $P_{a\alpha\beta}$ is an artificial viscous pressure [32]. We have assumed that classical collisions, which would tend to equilibrate the various component velocities [7, 3, 10, 25–27], are negligible. An artificial pressure is introduced so that the auxiliary equations will better mimic the true fluid equations, when fluid components are present. Its presence appears to have little significant effect under plasma PIC modeling.

A. Solution of the Maxwell-Moment System with Globally Implicit $\mathbf{v} \times \mathbf{B}$

We begin by making the pressure explicit, and the velocity in the $\mathbf{v}_\gamma \times \mathbf{B}$ term centered-implicit for the time integration of Eq. (5). Justification will be given in Subsection *a*. Thus, integrating, we obtain

$$\mathbf{j}_\alpha^{(m+1)} = \mathbf{j}_\alpha^{(m)'} + n_\alpha^{(m)} \varepsilon_\alpha \mathbf{E}^{(m+1)} + \mathbf{j}_\alpha^{(m+1)} \times \boldsymbol{\Omega}_\alpha \tag{6}$$

with $\mathbf{j}^{(m+1)} \equiv n^{(m)} \mathbf{v}^{(m+1)}$, $\mathbf{j}^{(m)'} \equiv \mathbf{j}^{(m)} - \nabla \cdot \bar{\mathbf{P}}^{(m)}\,\Delta t/m + \mathbf{j}^{(m)} \times \boldsymbol{\Omega}$, $\boldsymbol{\Omega} \equiv q\mathbf{B}^{(m)}\,\Delta t/2mc$, and $\varepsilon \equiv q\Delta t/m$. Operating from the right with the $\times \boldsymbol{\Omega}_\alpha$ and $\cdot\, \boldsymbol{\Omega}_\alpha$, we can rearrange Eq. (6) to

$$\mathbf{j}_\alpha^{(m+1)} = \mathbf{j}_\alpha^{(m)''} + n_\alpha^{(m)} \varepsilon_\alpha^{(m)} \frac{[\mathbf{E}^{(m+1)} + \mathbf{E}^{(m+1)} \times \boldsymbol{\Omega}_\alpha + (\mathbf{E}^{(m+1)} \cdot \boldsymbol{\Omega}_\alpha)\,\boldsymbol{\Omega}_\alpha]}{(1 + \Omega_\alpha^2)} \tag{7a}$$

with

$$\mathbf{j}_\alpha^{(m)''} = \frac{[\mathbf{j}_\alpha^{(m)'} + \mathbf{j}_\alpha^{(m)'} \times \boldsymbol{\Omega}_\alpha + (\mathbf{j}_\alpha^{(m)'} \cdot \boldsymbol{\Omega}_\alpha)\,\boldsymbol{\Omega}_\alpha]}{(1 + \Omega_\alpha^2)}, \tag{7b}$$

which expresses the new component fluxes $\mathbf{j}_\alpha^{(m+1)}$ in terms of the time advanced E-fields $\mathbf{E}^{(m+1)}$. Only the old, level-(m) densities and B-fields appear (through $\boldsymbol{\Omega}$) in this formulation. Formally, Eq. (7a) can be written

$$\mathbf{j}_\alpha^{(m+1)} = \mathbf{j}_\alpha^{(m)''} + \frac{\chi_\alpha}{4\pi q_\alpha\,\Delta t}\,\mathbf{E}^{(m+1)}, \tag{8}$$

in which the χ_α matrix is a component susceptibility.

Next, the component flux expressions are used with Ampere's law to relate the E-fields to $\nabla \times \mathbf{B}$. Substituting Eq. (8) into Eq. (4), we get after some rearrangement

$$\mathbf{E}^{(m+1)} = [\mathbf{I} + \chi]^{-1}\,\mathbf{E}^{(m)'} + [\mathbf{I} + \chi]^{-1}\,c\,\Delta t\,\nabla \times \mathbf{B}^{(m+1)}, \tag{9}$$

in which $\mathbf{I}$ is the unit diagonal matrix, $\chi \equiv \sum \chi_\alpha$ and $\mathbf{E}^{(m)'} \equiv \mathbf{E}^{(m)} - 4\pi \sum q_\alpha \mathbf{j}_\alpha^{(m)} \Delta t$. Combining this with Faraday's law, Eq. (2), one can acquire

$$\mathbf{B}^{(m+1)} = \mathbf{B}^{(m)} - c\,\Delta t\,\nabla \times [\mathbf{I}+\chi]^{-1}\,\mathbf{E}^{(m)'} + \nabla \times c^2\,\Delta t^2 [\mathbf{I}+\chi]^{-1}\,\nabla \times \mathbf{B}^{(m+1)}. \tag{10}$$

The solution to Eq. (10) with subsequent substitution into Eq. (9) would now complete our quest for an implicit field prediction. However, for a generally oriented B-field the formal inverse matrix $[\mathbf{I}+\chi]^{-1}$ is, perhaps, difficult to evaluate. Furthermore, it mixes the B-components in a most complex fashion, and so we seek simplification. We substitute Eq. (7a) into Eq. (4). This yields

$$\mathbf{E}^{(m+1)} = \mathbf{E}^{(m)'} + \sum \bar{\omega}_{p\alpha}^2\,\Delta t^2 [\mathbf{E}^{(m+1)} + \mathbf{E}^{(m+1)} \times \boldsymbol{\Omega}_\alpha + (\mathbf{E}^{(m+1)} \cdot \boldsymbol{\Omega}_\alpha)\,\boldsymbol{\Omega}_\alpha] + c\,\Delta t\,\nabla \times \mathbf{B}^{(m+1)}, \tag{11}$$

employing $\bar{\omega}_{p\alpha}^2 = \omega_{p\alpha}^2/(1+\Omega_\alpha^2)$ and $\omega_{p\alpha}^2 = 4\pi q_\alpha^2 n_\alpha / m_\alpha$. With the additional definitions $\bar{\omega}_{p0}^2 \equiv \sum \bar{\omega}_{p\alpha}^2$, $D \equiv (1+\bar{\omega}_{p0}^2)$, $\mathbf{E}^{(m)''} = \mathbf{E}^{(m)'}/D$, $\boldsymbol{\Omega}_\alpha \equiv \mathbf{U}\Omega_\alpha$ ($\mathbf{U}$ defining a unit vector along $\boldsymbol{\Omega}$), $\beta \equiv \sum \Omega_\alpha \bar{\omega}_{p\alpha}^2\,\Delta t^2$, $\varepsilon \equiv \sum \Omega_\alpha^2 \bar{\omega}_{p\alpha}^2\,\Delta t^2$ and $\gamma \equiv c\,\Delta t/D$, we convert Eq. (11) to

$$\mathbf{E}^{(m+1)} = \mathbf{E}^{(m)'} - \mathbf{E}^{(m+1)} \times \mathbf{U}\beta - (\mathbf{E}^{(m+1)} \cdot \mathbf{U})\,\mathbf{Y}\varepsilon + \gamma \nabla \times \mathbf{B}^{(m+1)}. \tag{12}$$

We now multiply both sides of Eq. (12) by the appropriate factors to form $(\mathbf{E}^{(m+1)} \cdot \mathbf{U})\,\mathbf{U}\varepsilon$ on the left of the equal sign. Rearrangement of the result provides an expression for the third term on the right of Eq. (12) in terms of $\mathbf{E}^{(m)''}$ and $\nabla \times \mathbf{B}^{(m+1)}$. Similarly, multiplication from the right with $\times \mathbf{U}$ (and $\cdot \mathbf{U}$) leads to an expression for the second term—following the Eq. (6)–(7a) model. Subsequent substitution of these results transforms Eq. (12) into

$$\mathbf{E}^{(m+1)} = \frac{\mathbf{E}^{(m)''} - \mathbf{E}^{(m)''} \times \mathbf{U}\beta + \gamma \nabla \times \mathbf{B}^{(m+1)} - \gamma \nabla \times \mathbf{B}^{(m+1)} \times \mathbf{U}\beta}{(1+\beta^2)} + \frac{[(\mathbf{E}^{(m)''} \cdot \mathbf{U}) + \gamma(\nabla \times \mathbf{B}^{(m+1)} \cdot \mathbf{U})]\,\mathbf{U}(\beta^2 - \varepsilon)}{(1+\beta^2)(1+\varepsilon)}. \tag{13}$$

This *general* expression for $\mathbf{E}^{(m+1)}$ in terms of $\nabla \times \mathbf{B}^{(m+1)}$ remains quite complex.

We note, however, that when the B-field is always perpendicular to the plane containing $\mathbf{E}$, then $\nabla \times \mathbf{B}$ is perpendicular to $\mathbf{B}$, and the last term in Eq. (13) is zero. Consequently, for ANTHEM we let $\mathbf{U} = \hat{\mathbf{k}}$, $\mathbf{B} = B_z \hat{\mathbf{k}}$, and $\mathbf{E} = E_x \hat{\mathbf{i}} + E_y \hat{\mathbf{j}}$ to produce the simplified component equations

$$E_x^{(m+1)} = \left(E_x^{(m)''} - \beta E_y^{(m)''} + \gamma \frac{\partial B_z^{(m+1)}}{\partial y} + \gamma\beta \frac{\partial B_z^{(m+1)}}{\partial x} \right) \Big/ (1+\beta^2) \tag{14a}$$

and

$$E_y^{(m+1)} = \left(E_y^{(m)''} + \beta E_x^{(m)'} - \gamma \frac{\partial B_z^{(m+1)}}{\partial x} + \gamma\beta \frac{\partial B_z^{(m+1)}}{\partial y} \right) \Big/ (1+\beta^2). \tag{14b}$$

These are combined with

$$B_z^{(m+1)} = B_z^{(m)} - c\,\Delta t\left[\frac{\partial E_y^{(m+1)}}{\partial x} - \frac{\partial E_x^{(m+1)}}{\partial y}\right] \tag{14c}$$

to yield a single elliptic equation for B_z.

a. Temporal Differencing

Let us now explore the consequences of our choices for the time levels of the various terms in the ANTHEM algorithm. We shall assume convergence of the predicted fields to the true fields. The iterative procedures that can lead to such convergence are discussed in Section 5. We look at linear stability for isothermal electrons, undergoing x–y planar oscillations in a uniform, motionless ion background, and in a prescribed ambient B_z-field. The mean electron thermal speed is $a_0 = (\kappa T/m)^{1/2}$, and $\omega_c = eB_z/mc$ is the gyrofrequency of electrons. We linearize Eqs. (2)–(5), assuming one-dimensional variations e^{ikx} and dependencies $j_x = j_{x1}e^{i\omega(t-t_0)} = j_{x1}e^{i\omega m\,\Delta t} = j_{x1}\xi^m$, for example. Thus, $j_y^{(m)} = j_{y1}\xi^m$, $E_x^{(m)} = E_{x1}\xi^m$, $E_y^{(m)} = E_{y1}\xi^m$, and $B_z^{(m)} = B_{z1}\xi^m$. Elimination of E_{x1}, j_{y1}, etc., from the resultant linear system leads to a sixth-order polynomial equation for ξ. The moduli of all the roots of this equation must satisfy $|\xi| \leqslant 1$ for numerical stability. The ANTHEM algorithm is useful when $\omega_p\,\Delta t > 1$. In this limit, from the ξ solutions we find that with *explicit* pressure

$$\frac{ka_0\,\Delta t}{(\omega_p\,\Delta t)} \leqslant 1 \tag{15a}$$

is needed for stability. This agrees with the Ref. [3] result. Equation (15a) can be weaker than the strict Courant limit, $ka_0\,\Delta t = a_0\,\Delta t/\Delta x \leqslant 1$, usually specified. With *centered implicit* $\mathbf{v}^{(*)} \times \mathbf{B}^{(m)}$ [i.e., $(*) = (m + 1/2)$] there is no time step constraint imposed by the magnetic field. Alternatively, with a *globally explicit*, $\mathbf{v}^{(m)} \times B$ term, Δt is constrained by the additional relation

$$M \equiv \frac{\omega_c\,\Delta t}{(\omega_p^2\,\Delta t^2)} \leqslant 1. \tag{15b}$$

Further scrutiny of the stability polynomial shows that electromagnetic waves are strongly damped with the simple $(\dagger) = (m+1)$, $\nabla \times \mathbf{B}^{(\dagger)}$ centering used here for exposition. The use instead of $(\dagger) \gtrsim (m + \frac{1}{2})$ in Eq. (4), and $\nabla \times \mathbf{E}^{(\dagger)}$ in Faraday's law, Eq. (14c), will minimize this damping. Relatedly, $(*) \gtrsim (m + \frac{1}{2})$ should be employed for the $\mathbf{j}^{(*)}$ currents in Eq. (4) to limit numerical damping of the plasma momenta.

b. Spatial Differencing and Storage

Equation (3a) is most readily modeled numerically by storing the densities at the cell centers, and the E_x and E_y fields at the mid-wall positions, as shown in Fig. 1.

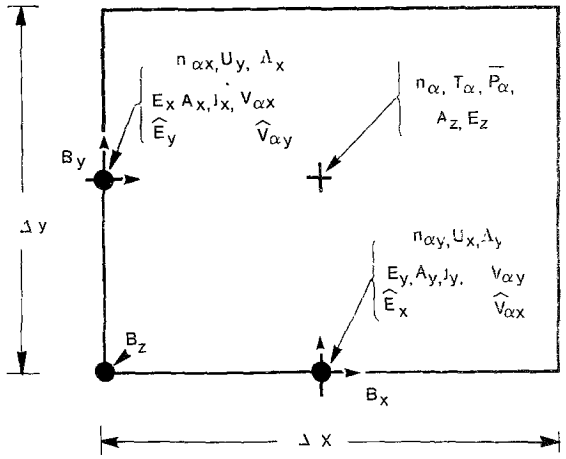

FIG 1. Storage conventions used in ANTHEM for a typical cell of width Δx and height Δy.

This allows convenient cell-centered positioning of the Eq. (3b) electrostatic potential ϕ. The placement of B_z at the cell corners (or nodes) [30, 2] then allows for simple differencing of Eq. (2). This is consistent with the storage of the A_x and A_y components at cell-wall midpoints, along with E_x and E_y, respectively. Finally, the j_x and j_y current components are stored at the mid-wall positions, facilitating the time advancement Ampere's law, Eq. (4). Pressures and temperatures are stored at cell centers. Since the E-fields and currents are stored at the wall midpoints, we define wall-averaged densities, for example, $n_{\alpha x} \equiv (n_{\alpha, l-1} + n_{\alpha, l})/2$, associated with the E_x and $v_y B_z$ terms, and let $v_{\alpha x} \equiv j_{\alpha x}/n_{\alpha x}$ in differencing Eq. (5). Similarly, $n_{\alpha y} \equiv (n_{\alpha, j-1} + n_{\alpha, j})/2$.

The elements of the Eq. (5) pressure tensor $\bar{\mathbf{P}}_\alpha$ are taken as $p_{\alpha x} \equiv mn\bar{v}_x^2 + P + P_{\alpha x}$, $P_{yy} \equiv mn\bar{v}_y^2 + P + P_{\alpha y}$, and $P_{xy} \equiv mn\bar{v}_x\bar{v}_y$ with the densities, pressures, and velocities evaluated at the time level-(m). The x-directed artificial viscous pressure is, for example, $P_{\alpha x} \equiv mn(v_{x,l} - v_{x,l+1})^2$, $v_{x,l} \geq v_{x,l+1}$, and zero otherwise. For the storage of the dynamic elements in the pressure components we have defined cell-centered velocities, e.g., $\bar{v}_{1x} \equiv (v_{x,l} + v_{x,l+1})/2$. The mesh-staggering of velocities and pressures has been imposed to assure the development of finite velocities in steep gradient regions. For example, the magnitude of isothermal static pressure driven velocity increments

$$\delta v_{1x} = -\frac{1}{mn}\frac{\partial P_{xx}}{\partial x}\Delta t = -\frac{(n_l - n_{l-1})}{(n_{l-1} + n_l)/2}\frac{\kappa T}{m}\frac{\Delta t}{\Delta x} \tag{16a}$$

is limited to the maximal value $(2\kappa T/m)$ $(\Delta t/\Delta x)$ (for n_l or $n_{l-1} \neq 0$). Had the velocities been stored along with the pressures at cell centers as in [16], the magnitude of the centered increments

$$\delta v_x = -\frac{(n_{l+1} - n_{l-1})}{n_l}\frac{\kappa T}{m}\frac{\Delta t}{\Delta x}$$

could grow without bound as, say, $n_i \to 0$. We, therefore, reject this alternate differencing. Similar considerations apply to the transverse P_{xy} gradients. Thus, at each node we define an average pressure from the four cells around the node, e.g., $P^{(\diamond)} \equiv (P_{i,j} + P_{i,j-1} + P_{i-1,j} + P_{i-1,j-1})/4$. Also, we compute corresponding nodal averaged densities $n^{(\diamond)}$. With these, the transverse increments are differenced as

$$\delta v_{2x} = -\frac{1}{mn}\frac{\partial P_{xy}}{\partial y}\Delta t = -\frac{1}{m(n_{i,j}^{(\diamond)} + n_{i,j+1}^{(\diamond)})/2}\frac{(P_{xy,i,j+1}^{(\diamond)} - P_{xy,i,j}^{(\diamond)})}{\Delta y}\Delta t. \quad (16b)$$

Again, this assures finite accelerations, if, alone, n_i or $n_{i-1} \to 0$. This may occur near a vacuum–plasma interface, or at an internal *hole* arising from the use of a limited number of particles in PIC simulation. The above discussion is heuristic. To allow for the future implementation of an r–z capability, and since, generally, $\Delta x \neq \Delta y$, the various density averages mentioned are, in fact, computed with volume weighted densities—effectively rendering them as mass averages. Combining these results, we use, for example,

$$-(\nabla \cdot \bar{\mathbf{P}})_{\alpha x}\,\Delta t/m_\alpha \equiv n_{\alpha x}(\delta v_{1\alpha x} + \delta v_{2\alpha x}) \quad (17)$$

in defining the x-component of the pressure tensor contribution to $\mathbf{j}_\alpha^{(m)'}$ for Eq. (6).

Although we store only the velocity and current components normal to the cell-wall faces, components parallel to the faces are needed as input to Eq. (7b) and for the calculation of the $\mathbf{E}^{(m)''}$ elements in Eqs. (14a) and (14b). We designate such parallel components with a hat, e.g., $\hat{\mathbf{v}}$ for the parallel velocities. See Fig. 1. To avoid the possibility of singularity in calculating such components, where, say, the $n_{x\alpha}$ are zero at an interface, while some of the v_α are nonzero, we mass average as for Eq. (16b), producing the supplemental component velocities $\hat{\mathbf{v}}_\alpha$. In the y direction, for example, these supplemental velocities are computed by the rule

$$\hat{v}_{y,i,j+1/2} \equiv \frac{(j_{y,i,j+1} + j_{y,i-1,j+1} + j_{y,i-1,j} + j_{y,i,j})/4}{(n_{i,j}^{(\diamond)} + n_{i,j+1}^{(\diamond)})/2}. \quad (18)$$

Again, the $j_y \equiv n_y \hat{v}_y$; in addition, cell volumes must multiply the densities for use in $\Delta x \neq \Delta y$ situations.

Next, for the $\mathbf{E}^{(m)''}$ of Eqs. (14) we need old E-components parallel to the walls. In the y direction along the left side of the cell we establish the level-(m) supplemental field by a simple average $\hat{E}_y \equiv (E_{y,i,j} + E_{y,i,j+1} + E_{y,i-1,j+1} + E_{y,i-1,j})/4$. Similarly along the bottom of the cell we use $\hat{E}_x \equiv (E_{x,i,j} + E_{x,i-1,j} + E_{x,i-1,j-1} + E_{x,i,j-1})/4$. Then, when Eq. (14) is differenced for the left cell wall, it gives the time level-$(m+1)$ component pair $(E_x, \hat{E}_y)$, while at the cell bottom it provides $(\hat{E}_x, E_y)$. Note that with B_z stored at the nodes, only the hat-free components of the E-field appear in the differenced form of Eq. (14c).

In forming the β and γ coefficients for Eqs. (14) we use the simple, nearest-node averages of $B_z^{(m)}$, i.e., $B_z^{(m)} \equiv (B_{z,i,j}^{(m)} + B_{z,i,j+1}^{(m)})/2$ along the left cell wall for the computation of $(E_x^{(m+1)}, \hat{E}_y^{(m+1)})$, and $B_z^{(m+1)} \equiv (B_{z,i,j+1}^{(m+1)} + B_{z,i,j+1}^{(m+1)})/2$ at the cell

bottom for the determination of $(\hat{E}_x^{(m+1)}, E_y^{(m+1)})$. The E-field-aligned $\nabla \times \mathbf{B}$ components in Eq. (14) are easily differenced. In Eq. (14a), for example, $\partial B_z/\partial y \equiv (B_{z,i,j+1} - B_{z,i,j})/\Delta y$. Calculation of the remaining components is a little more complex. We first construct cell-centered B_z-fields. Again, for Eq. (14a), $B_{z,i,j}^{(\diamond)} \equiv (B_{z,i,j} + B_{z,i+1,j} + B_{z,i+1,j+1} + B_{z,i,j+1})/4$. Then we use, for example, $\partial B_z/\partial x \equiv (B_{z,i,j}^{(\diamond)} - B_{z,i,j-1}^{(\diamond)})/\Delta x$. This implies the coupling of $B_{z,i,j}$ to the corner terms $B_{z,i\pm1,j\pm1}$.

c. *The B_z, E_x and E_y Determinations*

The more complex B-derivatives derive directly from the use of an implicit velocity in the differencing of the $\mathbf{v} \times \mathbf{B}$ in Eq. (5). They contribute nonsymmetrically to the matrix equation for B_z corresponding to Eq. (14). Thus, intrinsically, a 9-point, nonsymmetric elliptic solver is required for the B_z solution. For this we have used an ILUCG solver that was provided by Anderson [33] and improved and vectorized by Jordan [34, 35]. The ILUCG solver requires 19 full-mesh arrays and provides 15 solutions/s on a 50×50 mesh to an accuracy of 1 part in 10^6. Alternatively, we have employed a vectorized Chebycheff solver provided by Manteuffel [34, 35]. This is twice as fast, but requires 27 full-mesh arrays.

Once the B_z field has been determined by these procedures, the E-fields follow from substitution of B_z into Eqs. (14a) and (14b).

The globally implicit $\mathbf{v} \times \mathbf{B}$ formulation exists as an effective, working option for the determination of the fields in ANTHEM. However, the complexity of the algebra required to set up the coefficients for Eqs. (14), the need for a 9-point, nonsymmetric solver, and the difficulties in extending this approach into a full-field algorithm (with B_x, B_y, and E_z) has encouraged our development of an alternate, explicit magnetic approach.

B. *Explicit Magnetic* $\mathbf{v} \times \mathbf{B}$

In our simpler alternative approach the velocities for $\mathbf{v} \times \mathbf{B}$ are left *explicit* in *selective* aspects of the differencing. Thus, we integrate Eq. (5) formally to produce

$$\mathbf{j}_\alpha^{(m+1)} = \mathbf{J}_\alpha^{(m)} + n_\alpha^{(m)} \varepsilon_\alpha (\mathbf{E}^{(m+1)} + \mathbf{v}_\alpha^{(*)} \times \mathbf{B}^{(m)}/c) \tag{19}$$

with $\mathbf{J}^{(m)} \equiv \mathbf{j}^{(m)} - \nabla \cdot \bar{\mathbf{P}}\, \Delta t/m$. Then the formal substitution of Eq. (19) in Eq. (4) yields

$$\mathbf{E}^{(m+1)} = \frac{\mathbf{E}^{(m)} - 4\pi \sum q_\alpha \mathbf{J}_\alpha^{(m)}\, \Delta t - \sum \omega_{p\alpha}^2\, \Delta t^2 (\mathbf{v}_\alpha^{(*)} \times \mathbf{B}^{(m)})/c + c\, \Delta t\, \nabla \times \mathbf{B}^{(m+1)}}{(1 + \omega_{p0}^2\, \Delta t^2)}, \tag{20}$$

in which $\omega_{p\alpha}^2 \equiv 4\pi q_\alpha^2 n_\alpha^{(m)}/m_\alpha$ and $\omega_{p0}^2 \equiv \sum \omega_{p\alpha}^2$.

With only a single B_z component of the magnetic field and plasma motion and acceleration restricted to the x–y plane, the components of Eq. (20) can be written

$$E_x^{(m+1)} = E_{0x} - (U_y^{(*)} B_z^{(m)})/c + \left(\Lambda_x^2 \frac{\partial B_z^{(m+1)}}{\partial y} \right) \Big/ c\, \Delta t \tag{21a}$$

$$E_y^{(m+1)} = E_{0y} + (U_x^{(*)} B_z^{(m)})/c - \left(\Lambda_y^2 \frac{\partial B_z^{(m+1)}}{\partial x} \right) \Big/ c\, \Delta t, \tag{21b}$$

for which we have defined

$$\mathbf{E}_0 \equiv \frac{\mathbf{E}^{(m)} - 4\pi \sum q_\alpha \mathbf{J}_\alpha^{(m)} \Delta t}{(1 + \omega_{p0}^2 \Delta t^2)}, \tag{22a}$$

$$\mathbf{U}^{(*)} \equiv \frac{\sum \omega_{p\alpha}^2 \Delta t^2 \hat{\mathbf{v}}_\alpha^{(*)}}{(1 + \omega_{p0}^2 \Delta t^2)} \tag{22b}$$

and

$$\Lambda^2 \equiv \frac{c^2 \Delta t^2}{(1 + \omega_{p0}^2 \Delta t^2)}. \tag{22c}$$

Here, $\mathbf{E}_0$ is the reduced Eq. (20) for $\mathbf{B} = 0$. In one dimension it constitutes the implicit E-field solution for electrostatic problems [9, 12]. To calculate $\mathbf{U}$ and Λ, we evaluate the $\omega_{p\alpha}$ and ω_{p0} factors by using the wall averaged densities, $n_{x\alpha}$ for Eq. (21a) and $n_{y\alpha}$ for Eq. (21b), respectively. The velocities $\mathbf{U}$ run along the cell-wall surfaces (see Fig. 1) and are computed from the supplemental $\hat{\mathbf{v}}$ velocity components, such as given by Eq. (18). The $B_z^{(m)}$ for Eqs. (21) are evaluated as averages at the cell-wall centers.

Combination of Eqs. (21) and Faraday's law, Eq. (14c) yields

$$B_z^{(m+1)} - \frac{\partial}{\partial x} \left(\Lambda_y^2 \frac{\partial B_z^{(m+1)}}{\partial x} \right) - \frac{\partial}{\partial y} \left(\Lambda_x^2 \frac{\partial B_z^{(m+1)}}{\partial y} \right) = B_z^{(\dagger)} \tag{23a}$$

with

$$B_z^{(\dagger)} \equiv B_z^{(m)} - c \{ \nabla \times \mathbf{E}_0 \}_z \Delta t - \frac{\partial}{\partial x} (U_x^{(*)} B_z^{(m)}) \Delta t - \frac{\partial}{\partial y} (U_y^{(*)} B_z^{(m)}) \Delta t. \tag{23b}$$

The bracket's z subscript refers to the only nonzero component resulting from vector operations in Eq. (23a).

a. Our Choices for $\mathbf{v}^{(*)}$

With $(*) \equiv (m + \frac{1}{2})$ the flux equation, Eq. (19), reduces to Eq. (6) with the E-dependent solution, Eq. (7). We use the equivalent of these expressions to advance the plasma velocities, as detailed in the next section. There, the implicit choice for $\mathbf{v}$ assures us that the component fluxes and velocities will be finite, regardless of the magnitude of $\Omega_\alpha \Delta t$.

Similarly, the choice $(*) \equiv (m + \frac{1}{2})$ in Eq. (20) for the E-field produces an

expression that can be rearranged to yield Eq. (13). Changes in $\nabla \times \mathbf{B}$ can then generate both parallel and orthogonal changes in $\mathbf{E}$. In all the problems run thus far with ANTHEM, we find, however, that the explicit choice $(*) \equiv (m)$ in Eq. (21) is, in fact, sufficient to yield physically plausible results, in essential agreement with those from the more complex implicit procedure.

Finally, by making the explicit choice $(*) = (m)$ in Eq. (23b), we are led to the relatively simple 5-point elliptic Eq. (23a) for B_z. We take the view that $(*) = (m)$ in Eq. (23b) is the first choice of an iterative procedure leading to the proper implicit selection, $(*) = (m + \frac{1}{2})$. For the simple case of a single B-component and planar cross-field plasma motions, analysis shows this iterative process to be stable for arbitrary values of the magnetic stability parameter M of Eq. (15b). This is a consequence of the fact that perturbations in B_z drive velocity changes that are principally orthogonal to the direction of B-field advection from the $\mathbf{v} \times \mathbf{B}$ term. In practice, we have found no instance when the B-fields from this simpler algorithm differed in any substantive way from those derived via the more complex globally implicit equations.

b. Solution to the Simplified B_z Equation

To complete the field solution we simply carry out the explicit Eq. (23b) updates, producing $B_z^{(\dagger)}$, and then treat the resultant Eq. (23a) expression with an elliptic equation solver. The last two terms in Eq. (23b) represent advection of $B_z^{(m)}$ with the velocity $\mathbf{U}$. To avoid numerical instability we have used donor-cell spatial differencing [36]. The addition of Van Leer corrections [3, 28] would render the B-field advection with less numerical diffusion. When the time step is set to obey a Courant condition on the hottest electron component, it follows that $U_\beta \, \Delta t \leqslant \Delta x_\beta$, so that we can advect the *old*, level-(m) B-field. Equation (23a) exhibits five-point symmetric coupling of B_z at the node i, j to B_z at the neighboring nodes $i \pm 1, j$ and $i, j \pm 1$. It is readily inverted with an ICCG solver [37] once $B_z^{(\dagger)}$ is known. We simply invert the matrix equation $\tilde{\mathbf{M}} \mathbf{B}_z^{(m+1)} = \mathbf{B}_z^{(\dagger)}$ for the unknown elements $B_z^{(m+1)}$. For this we have used the decendent of a solver provided by Kershaw [38], modified and vectorized at Los Alamos by Jordan [34]. The ICCG solver can accomodate symmetric elliptical problems with 9-point discretization. It requires only 15 full-mesh arrays and equals the speed of the more core-demanding Chebycheff solver.

With B_z determined, $\mathbf{E}$ can be determined from Eqs. (14a) and (14b) [equivalent to using $(*) \equiv (m + \frac{1}{2})$ in Eq. (21)]. However, we have found it simpler and sufficient to use Eq. (21) directly with $(*) \equiv (m)$.

c. Physical Interpretation

For large $\omega_{p0} \, \Delta t$ the $\mathbf{E}_0$ of Eq. (22a) reduces to $-(1/en_e) \nabla (n_o \kappa T_e)$ (assuming negligible electron drift). Thus, the second term on the right side of Eq. (23b) can represent a thermo-electric source, going as $\nabla n_e \times \nabla T_e$, for new B-field [39, 40]. The last two terms represent advection of B_z with the fluid components. Finally, the

partial derivative terms in Eq. (23a) imply a dispersion or separation [41] of the advected B_z from the moving fluid elements over the skin depth Λ. Alternatively, in tenuous plasmas, for which $\omega_{p0}\,\Delta t \ll 1$, Eq. (22a) limits as $\mathbf{E}_0 \to \mathbf{E}^{(m)}$ since remaining fluidic terms in Eq. (13a) are small and $\Lambda \to c\,\Delta t$, so that Eqs. (23) reduce to a model for the propagation of light.

For large time steps (and ions moving no faster than the electrons) the effective velocity $\mathbf{U}$ reduces essentially to the electron velocity, $\mathbf{U} \to \mathbf{v}_e$, where $\mathbf{v}_e \equiv (n_c\mathbf{v}_c + n_h\mathbf{v}_h)/(n_c + n_h)$. Also, for large Δt our Λ becomes the electromagnetic skin depth c/ω_{p0}. Moreover, Eqs. (4) and (19) give $v_{ey} \to (c/4\pi e n_e)(\partial B_z/\partial x)$ in this limit, so that the ions in one-dimensional x-directed problems, are, for example, accelerated by

$$E_x = -\frac{1}{en_e}\frac{\partial}{\partial x}\left(n_e \kappa T_e + \frac{B_z^2}{8\pi}\right), \tag{24}$$

as employed in the early magnetosonic shock propagation studies of Ref. [35].

d. Applicability of the Simpler Scheme

In all the problem thus for examined with ANTHEM no significant difference has been observed in the results obtained with either the "globally implicit," or the "magnetic explicit" modes of the field algorithm. Thus, no difference was seen in the demonstrative calculations at the end of this paper, in our recent calculations of the Nernst advection of B-field in collisional plasmas [42], or in our recent computations of the plasma dynamics in a Plasma Erosion Switch [43] (run for the Eq. (15b), M exceeding 20). The explicit magnetic approach should be attractive, due to its relative simplicity. But its chief value may lie in its possible extension to full-field problems. While Faraday's law generates a most complex system from Eq. (13), the explicit magnetic approach yields the apparently more tractible procedure of the next section.

C. The Full-Field Algorithm

The explicit magnetic $\mathbf{v} \times \mathbf{B}$ approach is readily extended to provide straightforward solutions for problems in which all the six field components (E_x, E_y, E_z, B_x, B_y and B_z) are active. For this extension A_z, E_z, j_z, and v_z are all defined at cell centers, B_x is stored at the bottom cell-wall midpoint, B_y is kept at the left side cell-wall midpoint, and $\partial/\partial z$ remains zero. Motions along the B-field components are allowed, and the pressure tensor is generalized accordingly. The components of Eq. (20) then become

$$\mathbf{E}^{(m+1)} = \mathbf{E}_{00} + \frac{c\,\Delta t}{\mathbf{K}}\left\{\frac{\partial B_z^{(m+1)}}{\partial y}\hat{\mathbf{i}} - \frac{\partial B_z^{(m+1)}}{\partial x}\hat{\mathbf{j}} + \left(\frac{\partial B_y^{(m+1)}}{\partial x} - \frac{\partial B_x^{(m+1)}}{\partial y}\right)\hat{\mathbf{k}}\right\}, \tag{25}$$

with $\mathbf{E}_{00} \equiv \mathbf{E}_0 - \mathbf{U}^{(m)} \times \mathbf{B}^{(m)}/c$ from Eqs. (20) and (22), and $K \equiv 1 + \omega_{p0}^2\,\Delta t^2$. At the beginning of a time step $\mathbf{E}_{00}$ is completely known.

Equation (25) can be combined with Faraday's law to produce the three component equations

$$B_x^{(m+1)} = B_x^{(m)} - c\,\Delta t\{\nabla \times \mathbf{E}_{00}\}_x - c\,\Delta t \frac{\partial}{\partial y}\left\{\frac{1}{K}\left(\frac{\partial B_y^{(m+1)}}{\partial x} - \frac{\partial B_x^{(m+1)}}{\partial y}\right)\right\}, \quad (26a)$$

$$B_y^{(m+1)} = B_y^{(m)} - c\,\Delta t\{\nabla \times \mathbf{E}_{00}\}_y + c\,\Delta t \frac{\partial}{\partial x}\left\{\frac{1}{K}\left(\frac{\partial B_y^{(m+1)}}{\partial x} - \frac{\partial B_x^{(m+1)}}{\partial y}\right)\right\}, \quad (26b)$$

and

$$B_z^{(m+1)} = B_z^{(m)} - c\,\Delta t\{\nabla \times \mathbf{E}_{00}\}_z - c\,\Delta t\left\{\frac{\partial}{\partial x}\left(\frac{1}{K}\frac{\partial B_z^{(m+1)}}{\partial x}\right) + \frac{\partial}{\partial y}\left(\frac{1}{K}\frac{\partial B_z^{(m+1)}}{\partial y}\right)\right\}. \quad (26c)$$

The B_z equation is equivalent to Eqs. (23), except that additional coupling to B_x and B_y is included *explicitly* in the $\sum \omega_{p0}^2\,\Delta t^2(\mathbf{v}_\alpha^{(m)} \times \mathbf{B}^{(m)})/c$ term of $\mathbf{E}_{00}$. As with the earlier, Section B more restrictive version of the algorithm, a solution for $B_z^{(m+1)}$ is easily achieved with an ICCG solver.

The remaining B_x, and B_y equations are strongly coupled, and through elimination would lead to separate fourth-order equations beyond the capabilities of our elliptic solvers. We, therefore, bypass these equations and turn instead to the vector potentials.

We return to Ampere's law, expressed in terms of $\mathbf{A}$ and ϕ with the aid of Eqs. (3). Setting $(*) = (m+1)$ in Eq. (4) and letting $\nabla \cdot \mathbf{A} = 0$ for the Coulomb gauge, we obtain

$$\frac{-\mathbf{A}^{(m+1)} + 2\mathbf{A}^{(m)} - \mathbf{A}^{(m-1)}}{c\,\Delta t} + c\,\Delta t\,\nabla^2\mathbf{A}^{(m+1)} = \nabla\phi^{(m+1)} - \nabla\varphi^{(m)} - 4\pi\sum q_\alpha \mathbf{j}_\alpha^{(m+1)}\,\Delta t. \quad (27)$$

Next, summing over the components of Eq. (19) [here, with $(*) \equiv (m)$], we produce

$$4\pi\sum_\alpha q_\alpha \mathbf{j}_\alpha^{(m+1)}\,\Delta t = -4\pi\sum_\alpha \mathbf{I}_\alpha \mathbf{A}_\alpha^{(m)} - \omega_{p0}^2\,\Delta t^2\left(\nabla\phi^{(m+1)} - \frac{1}{c}\frac{\partial \mathbf{A}}{\partial t}\right)^{(m+1)}$$

$$- \sum \omega_{p\alpha}^2\,\Delta t\left(\frac{\mathbf{A}^{(m+1)} - \mathbf{A}^{(m)}}{c}\right). \quad (28)$$

Substitution of the Eq. (28) flux sum into Eq. (27) then yields

$$\mathbf{A}^{(m+1)} - \frac{c^2\,\Delta t^2\,\nabla^2\mathbf{A}^{(m+1)}}{(1+\omega_{p0}^2\,\Delta t^2)} = \mathbf{A}^{(m)} - c\,\Delta t\,\nabla\phi^{(m+1)} - c\,\Delta t\,\mathbf{E}_{00}. \quad (29a)$$

We need only the z component of Eq. (29a), which is decoupled from ϕ, i.e.,

$$A_z^{(m+1)} - \frac{c^2 \Delta t^2}{K} \nabla^2 A_z^{(m+1)} = A_z^{(m)} - c \Delta t \{\mathbf{E}_{00}\}_z. \tag{29b}$$

This elliptic equation is symmetric and readily solved with our ICCG package for A_z. Then,

$$B_x^{(m+1)} = \frac{\partial A_z^{(m+1)}}{\partial y} \tag{30a}$$

and

$$B_y^{(m+1)} = -\frac{\partial A_z^{(m+1)}}{\partial x}. \tag{30b}$$

For maximum stability of the algorithm the E-fields should be obtained from Eq. (13), although the direct use of Eq. (25) may suffice (as does $(*) \equiv (m)$ for Eqs. (21) in the restricted $\mathbf{B} = B_z \hat{\mathbf{k}}$ case).

For numerical stability with the explicit coupling terms, i.e., $\nabla \times (\mathbf{U}^{(m)} \times \mathbf{B}^{(m)}) \Delta t$ in $c \Delta t \nabla \times \mathbf{E}_{00}$ of Eqs. (26), we must respect a Courant-like time step limit

$$\Delta t < \frac{\min[\Delta x, \Delta y]}{\max[|U_x|, |U_y|, |U_z|]}. \tag{31}$$

In our experience, limited to a single B-field component, we have used the more stringent rule obtained with $\max[|\mathbf{v}|_\alpha]$ replacing $\mathbf{U}$. The expanded coupling term includes elements of the form $\partial(v_\alpha B_\beta)/\partial x_\alpha$. These should be modeled with donor-cell or Van Leer differencing for additional stability.

We can report that in recent full-field applications of the alternate VENUS code algorithm [18] to the Weibel instability problem [44], no noticeable changes were observed [45], when velocities in the VENUS $\mathbf{v} \times \mathbf{B}$ term were switched from implicit to explicit values. However, our full-field extension has *not* yet been tested in ANTHEM. In the very least, it should be reliable for weak B-field problems ($M \leqslant 1$), where it could certify the results of more complex algorithms [16, 20].

4. Plasma Advancement

A. Particle Motion

Once the advanced fields have been calculated for any computational cycle, the velocity $\mathbf{u}_l$ and position $\mathbf{x}_l$ of any collisionless PIC particles used to represent a plasma component can be advanced in accordance with Newton's Laws

$$\frac{d\mathbf{u}_l}{dt} = \frac{q_l}{m_l}\left(\mathbf{E} + \frac{\mathbf{u}_l \times \mathbf{B}}{c}\right) \tag{32a}$$

$$\frac{d\mathbf{x}_l}{dt} = \mathbf{u}_l. \tag{32b}$$

We difference these as

$$\mathbf{u}_l^{(m+1)} = \mathbf{u}_l^{(m)} + \frac{q_l}{m_l}\left(\mathbf{E}^{(m+1)} + \frac{\mathbf{u}_l^{(m+1/2)} \times \mathbf{B}^{(m)}}{c}\right)\Delta t \tag{33a}$$

$$\mathbf{x}_l^{(m+1)} = \mathbf{x}_l^{(m)} + \mathbf{u}_l^{(m+1/2)}\,\Delta t. \tag{33b}$$

The velocities are centered in Eq. (33a) to assure energy conservation in the gyromotions.

For each particle l the solution to Eq. (33a) can be written

$$\mathbf{u}_l^{(m+1)} = \mathbf{u}_l^{(m)'} + \varepsilon_l \frac{[\mathbf{E}^{(m+1)} + \mathbf{E}^{(m+1)} \times \boldsymbol{\Omega}_l + (\mathbf{E}^{(m+1)} \cdot \boldsymbol{\Omega}_l)\,\boldsymbol{\Omega}_l]}{(1+\Omega_l^2)} \tag{34a}$$

with

$$\mathbf{u}_l^{(m)''} = \frac{[\mathbf{u}_l^{(m)} + \mathbf{u}_l^{(m)} \times \boldsymbol{\Omega}_l + (\mathbf{u}_l^{(m)} \cdot \boldsymbol{\Omega}_l)\,\boldsymbol{\Omega}_l]}{(1+\Omega_l^2)} \tag{34b}$$

and $\varepsilon_l \equiv q_l\,\Delta t/m_l$. For stability and accuracy the E- and B-fields should be evaluated at the advanced level-$(m+\frac{1}{2})$ particle positions. These positions can be found by the Newton–Raphson iteration of Eqs. (33b) and (34). The iteration procedure is outlined for one-dimensional problems in Ref. [3]. Typically, three iterations are sufficient to isolate the positions to one part in 10^3.

Clearly, the accelerations, Eq. (34), experienced by a particle which just happens to be located at a cell-wall center are very similar in form to the accelerations, Eqs. (7), experienced by the corresponding auxiliary fluid at the same points. That is, each cell-wall center point may be thought of as a particle of wall-averaged mass accelerating in the local fields. A difference is that the fluid velocities $\mathbf{v}^{(m)'}\,[\equiv \mathbf{j}^{(m)''}/n^{(m)}]$ include an increment due to the pressure gradients, which is, of course, lacking in $\mathbf{u}^{(m)''}$ of the particle update expressions.

As the final position of each particle is determined, we add its contribution to the local cell-centered density, currents, and pressures of the component it represents. The usual bilinear interpolation procedure (or area-weighting) [1] is used to attribute the particle contribution to its neighboring four cells. The components P_{xx}, P_{yy}, and P_{xy} are accumulated directly for use in Eq. (6). Currents $\mathbf{j}$ attributed to the cell-wall centers for Eqs. (14) and (20) are determined from averages of the accumulated cell centered values $\hat{\mathbf{j}}$. For example, $j_{xx} \equiv (\hat{j}_{xx,\,i-1,\,j} + \hat{j}_{xx,\,i,\,j})/2$, such

that, again, $v_{\alpha x} \equiv j_{\alpha x}/n_{\alpha x}$. Also, the E- and B-fields are first averaged to the cell centers before they are weighted to the particle positions—to eliminate self-forces.

The area-weighted currents accumulated by these procedures will satisfy flow continuity in some sense, but generally not in detail. This can cause difficulty in accurately determining implicit fields consistent with Poisson's Eq. (3a). Consequently, an additional set of *true* currents $\mathbf{j}$ is determined by precisely accounting for the density changes in neighboring cells as each particle moves within or across cell boundaries during a time step. The construction of these improved currents was first discussed by Morse and Nielson [46]. We use a variant of this construction procedure that was recently designed by Gisler and Jones [47] for use in a relativistic implicit PIC algorithm [48]. In Section 5 we show how these improved currents can be used to provide important corrections to the fields.

B. True Fluids Update

In hybrid modeling one or more of the plasma components is treated as a it true fluid. Such components are advanced via a continuity equation

$$\frac{\partial n_\alpha}{\partial t} = -\nabla \cdot [n_\alpha \mathbf{v}_\alpha], \tag{35a}$$

a momentum equation, the equivalent of Eq. (5), and an energy equation

$$\partial[(\tfrac{3}{2}\kappa T_\alpha)\, n_\alpha]/\partial t = -\nabla \cdot [(\tfrac{3}{2}\kappa T_\alpha)\, n_\alpha \mathbf{v}_\alpha)] - P_\alpha \nabla \cdot \mathbf{v}_\alpha - \nabla \cdot \mathbf{q}_\alpha. \tag{35b}$$

For the heat flux $\mathbf{q}_\alpha$ in Eq. (26b) we use Braginskii's expressions [31], flux-limited to assure that, for example, electron thermal energy is transported no faster than the mean electron thermal speed.

Strictly speaking, use of the fluid modeling can only be justified when the plasma component is in some fashion sufficiently collisional to maintain a nearly isotropic distribution among its elements. This might occur from turbulence, reflection off confining B- or self-consistent E-fields, or simply from classical collisions. We have, however, neglected classical collisional coupling between the components in the present development. The implementation of collisional effects is outlined elsewhere [26]. Formally, we can close the system of Eqs. (5) and (35) with the assumption $P_\alpha = n_\alpha \kappa T_\alpha$. The results from fluid modeling in collisionless regions can then, at least, be used as a basis for comparison with the results from more complete particle simulations.

Following Gentry *et al.* [36], DeBar [49], Sutcliffe [50], and Youngs [51], we split the hydrodynamic update into a Lagrangian phase and a remap phase. During the Lagrangian phase we accelerate the cell-wall midpoints under the action of the pressure gradients and fields and then move these points to new positions in accordance with the new midpoint velocities. During this move the cell densities can rise or fall. Correspondingly, the component temperatures can increase or decrease through the action of hydrodynamic work. Then, in the advection (or remap) phase

the walls are slipped back to their original positions on the Eulerian mesh, and the component materials are allowed to cross the walls into the neighboring cells.

The new velocities for the Lagrangian phase are obtained, using centered implicit velocities in the $\mathbf{v} \times \mathbf{B}$ terms, as for Eqs. (7) and (19). These velocities are identical to those that would come from Eqs. (7) with $\mathbf{v}_\alpha = \mathbf{j}_\alpha / n_\alpha$, except that the dynamic terms, i.e., $m_\alpha n_\alpha v_\beta v_\alpha$, are omitted from the pressure tensor. (The dynamic terms contribute to an estimate of advective effects in the field solution; these effects are recovered in the second phase of the hydrodymic advancement procedure.) At the left cell-wall center we compute the pair $(v_x, \hat{v}_y)$, and at the cell bottom we calculate $(\hat{v}_x, v_y)$. Only the values v_x and v_y are then used to move the cell walls. With these new Lagrangian velocities (henceforth designated with a tilde, e.g., $\tilde{v}_{\alpha x}$), we proceed to update each fluid component in turn. For each, the operations are split into separate x- and y-directed one-dimensional problems. In a given cycle the x direction may be updated first, followed by the y direction. In the next cycle this order is reversed. The flow in each direction is treated in accordance with the *Fluids Update* discussion of Ref. [3].

Completing the Lagrangian phase of the α-fluid in the x direction, for example, we move all the cell boundaries, in accordance with the $\tilde{v}_{\alpha x}$ values, from $x_i^{(m)}$ to temporary positions $\tilde{x}_i$, for a change δx_i. The new Lagrangian densities then become $\tilde{n}_\alpha = n_\alpha^{(m)}(\Delta x^{(m)}/\Delta \tilde{x})$ with $\Delta x \equiv x_{i+1} - x_i$. Correspondingly, the hydrodynamic work term in Eq. (35b) produces the temporary new temperatures, $\tilde{T}_\alpha = T_\alpha^{(m)} - P'_\alpha(\partial v_{\alpha x}/\partial x)\,\Delta t$, in which P' includes the x directed artificial viscous pressure $P_{\alpha x}$. For maximal accuracy with stability the temporary positions should be located through the use of an additional predictor-corrector step, by which the old pressure gradients and fields at the old positions are first used to provide accelerations to half-time velocities and positions, with this data subsequently employed to provide the pressures and fields for a final acceleration and advancement to the end of the time step. At present, our algorithm neglects this extra correction.

In the follow-on remap phase for component-α, we advect first density, then temperature, and finally the two components of velocity. As each vertical cell wall is returned to its initial position, a flux

$$\check{J}_x \equiv (\delta x/\Delta t)\,\check{n}_\alpha = \tilde{v}_x \check{n}_\alpha \tag{36a}$$

crosses the wall. In the density advection calculation second-order accuracy is approached by using Youngs' [51] extrapolation

$$\check{n}_\alpha = \tilde{n}_\alpha + \tfrac{1}{2}(1 - u)\,D\,\Delta x \tag{36b}$$

containing D allows for a density gradient near the donating cell. The purely second-order choice $D = \bar{D} \equiv (\tilde{n}_i - \tilde{n}_{i-1})/\Delta x$ can give rise to nonphysical maxima and minima in the solution. Consequently, nonlinear limits are set on D which guarantee monotonicity, while minimizing numerical diffusion. The limiter used is

$$D\,\Delta x \equiv R \min(|\bar{D}\,\Delta x|, 2|\tilde{n}_d - \tilde{n}_u|, 2|\tilde{n}_u - \tilde{n}_r|), \tag{36c}$$

for which $R=0$ if $\text{sgn}(\tilde{n}_d-\tilde{n}_u)\neq\text{sgn}(\tilde{n}_u-\tilde{n}_r)$, and $R=\text{sgn}(\tilde{n}_d-\tilde{n}_u)$ otherwise. Also, $d\equiv i$ with $r\equiv i-2$, if $\tilde{v}_x>0$, and $d\equiv i-1$ with $r\equiv i+1$, if $\tilde{v}_x<0$. More details are given in Ref. [3]. The Van Leer method [28] used here, as interpreted by Youngs [51], is akin to the FCT approach of Book *et al.* [52], except that the diffusion corrections are made as an integral part of the advection update, rather than in the separate antidiffusion step that is characteristic of FCT. The new density following the x directed advection is

$$\dot{n}_x^{(m+1)}=[\tilde{n}\,\Delta\tilde{x}+(\check{J}_{x,\,i}-\check{J}_{x,\,i+1})\,\Delta t]/\Delta x. \tag{36d}$$

Similarly, as the vertical walls are restored to their starting positions, they are crossed by a flux of specific energy $\delta\varepsilon\equiv\check{J}_x\check{T}$, leading to the new temperature

$$\dot{T}^{(m+1)}=[\tilde{n}\,\Delta\tilde{x}\tilde{T}+(\delta\varepsilon_i-\delta\varepsilon_{i+1})\,\Delta t]/(n\,\Delta x). \tag{37}$$

The fluxed $\check{T}$ value is determined from Eq. (36b) by substituting T for n and letting $\eta=\min(|\check{J}_x|\,\Delta t/(n\,\Delta x)_u,\,1)$. Again, u indicates the donating cell.

Next, for the advection of the longitudinal v_x velocities, we construct the cell-centered fluxes $\check{J}'_x\equiv(\check{J}_{x,\,i-1}+\check{J}_{x,\,i})/2$ and $\delta\Phi\equiv\check{J}'_x\check{v}_x$, and we determine that

$$\dot{v}_x^{(m+1)}=[\tilde{n}_x\,\Delta\tilde{x}\tilde{v}_x+(\delta\Phi_i-\delta\Phi_{i+1})\,\Delta t]/(n_x\,\Delta x), \tag{38}$$

with $\check{v}_x$ derived from Eq. (36b) by changing n to v_x with $\eta\equiv\min(|\check{J}'_x|\,\Delta t/(n_x\,\Delta x)_u,\,1)$.

Finally, the transverse velocity component v_y is advected with the averaged flux $\check{J}''_x\equiv(\check{J}_{x,\,i,\,j}+\check{J}_{x,\,i,\,j-1})/2$. To produce $\check{v}_y$ we change n to v_y in Eq. (36b) and use the definition $\eta\equiv\min(|\check{J}''_y|\,\Delta t/(n_y\,\Delta x)_u,\,1)$. Then we construct the average specific momentum flux $\delta\Upsilon\equiv\check{J}''_x\check{v}_y$, which allows us to complete the x-directed advection with the result

$$\dot{v}_y^{(m+1)}=[\tilde{n}_y\,\Delta\tilde{x}\tilde{v}_y+(\delta\Upsilon_i-\delta\Upsilon_{i+1})\,\Delta t]/(n_y\,\Delta x). \tag{39}$$

A corresponding set of updates is then made, starting, for example, with the intermediate $\dot{n}$ property, to calculate the effects on each of the moments of the y-directed advection.

Special care must be taken at the matter–vacuum interface for each of the fluids. Boundary densities n_x and n_y below a floor value n_{vac} are considered vacuum densities. We set $\tilde{v}_x$, for example, to zero, when $n_x^{(m)}<n_{\text{vac}}$. Typically, n_{vac} is set four decades below any physically important density in a problem. The Eq. (36b) η values are set to unity in the boundary cells to assure donor-cell advection up to the vacuum interface. Also, the static and artificial pressures are set to zero in any compressive cells bordering the vacuum to avoid erroneous numerical hydrodynamic heating of the edge material. In Ref. [3] we recommended the implementation of entropy advection, in lieu of internal energy advection, to avoid the numerical edge heating. While this was generally effective, it was not readily

extended to imperfect gases or the usual tabulated equations of state. Thus, here we return to more standard procedures. The additional use of volume-of-fluid (VOF) techniques [53, 54] is contemplated for a more refined modeling of the vacuum boundary.

Following the advection updates, an implicit evaluation of $\frac{3}{2}n_\alpha\kappa(\partial T_\alpha/\partial t) = -\nabla\cdot\mathbf{q}_\alpha$ permits the determination of additional T_α changes due to the last term in Eq. (35b). Thus, we can model the effects of flux-limited thermal conduction.

The availability of fluid modeling is particularly useful in treating plasmas with steep density gradients, which might otherwise require a very large number of simulation particles to represent the dense side of an interface. Such steep density gradient regions are prominent in CO_2 laser-driven transport problems near the critical surface [55] where the laser light is absorbed.

5. Field Corrections

In the straightforward application of the Section 3 algorithms to steep-gradient laser driven problems, we have found that, while the calculated B-fields are physically quite plausible, the E-fields must be in error, since the electrons gradually separate from the ions, spreading over many Debye lengths into the adjacent low density regions. Our implicit scheme should minimize such nonphysical separation by manifesting sufficient charge separation related E-field components to pull the electrons back to quasi-neutral positions. However, the basic Section 3 algorithms will fail to manufacture such corrective fields, since Eq. (4) makes no direct reference to the charge densities, and since the currents employed in Eq. (4) will generally fail to obey fluid continuity in detail.

More specifically, from Eq. (35a) after referencing the old plasma densities $\check{n}_\alpha^{(m)}$ we can produce the time-integrated *auxiliary continuity equations*

$$n_\alpha^{(m+1)} = \check{n}_\alpha^{(m)} - \nabla\cdot\mathbf{j}_\alpha^{(m+1)}\,\Delta t. \tag{40}$$

Given the implicit field solutions for any computational cycle, Eqs. (19) will generate predicted currents, which can be placed in Eq. (40) to provide predicted densities. It is these *predicted* densities $n_\alpha^{(m+1)}$ that will differ, in general, from the *true* densities $\check{n}_\alpha^{(m+1)}$ that accumulate after the particles and/or true fluids have advanced. The two densities will differ because, for example, the Eq. (19) currents are determined from spatially centered average densities and fields evaluated at the cell-wall centers, while the true plasma advancement uses particles that are accelerated in area weighted fields and fluid currents calculated with Van Leer averaged densities.

A. The Longitudinal E-Field Correction

In devising a correction for the difference between the densities predicted each cycle and the densities actually achieved, it is first useful to observe that the E-field

can be divided into longitudinal (irrotational) and transverse (rotational) parts, i.e., $\mathbf{E} = \mathbf{E}_l + \mathbf{E}_t$ with $\nabla \times \mathbf{E}_l = 0$ and $\nabla \cdot \mathbf{E}_t = 0$. Also, note that in Coulomb gauge (for which $\nabla \cdot \mathbf{A} = 0$) $\nabla \cdot \mathbf{E} = \nabla \cdot \mathbf{E}_l = -\nabla^2 \phi$ [56].

Focusing now on the longitudinal E-field component, we take the divergence of Eq. (4), obtaining

$$\nabla \cdot \mathbf{E}^{(m+1)} = \nabla \cdot \mathbf{E}^{(m)} - 4\pi \sum q_\alpha \nabla \cdot \mathbf{j}_\alpha^{(m+1)} \Delta t. \tag{41a}$$

Substitution for $\nabla \cdot \mathbf{E}$ from Eq. (3a) then gives

$$\sum q_\alpha n_\alpha^{(m+1)} = \sum q_\alpha n_\alpha^{(m)} - \sum q_\alpha \nabla \cdot \mathbf{j}_\alpha^{(m+1)} \Delta t. \tag{41b}$$

Equation (41b) will agree with the sum of the Eq. (40) components, and the predicted E-field will act to correct the charge separation errors just discussed, if we make the change $\mathbf{E}^{(m)} \to \mathbf{E}^{(m)'} \equiv \mathbf{E}^{(m)} + \delta \mathbf{E}_l^{(m)}$ in Eqs. (4) and (20), such that

$$\nabla \cdot \mathbf{E}^{(m)'} = 4\pi \sum q_\alpha \check{n}_\alpha^{(m)}. \tag{42}$$

This is accomplished by letting

$$\nabla \cdot \delta \mathbf{E}_l^{(m)} = -\nabla^2 \delta \phi^{(m)} = 4\pi \sum q_\alpha \check{n}_\alpha^{(m)} - \nabla \cdot \mathbf{E}^{(m)}. \tag{43}$$

The solution $\delta \phi^{(m)}$ to this Poisson equation is readily determined using the FISHPAK routines of Adams, Swarztrauber, and Sweet [57, 58]. Then, $\delta \mathbf{E}_l^{(m)} = -\nabla \delta \phi^{(m)}$, and

$$\mathbf{E}^{(m)'} = \mathbf{E}^{(m)} - \nabla \delta \phi^{(m)}. \tag{44}$$

This is equivalent to the one-dimensional field correction introduced by Denavit [13].

Integrating Eq. (42), we see that for one-dimensional electrostatic ($\mathbf{B} = 0$) problems with, say, reflecting boundaries at $x = 0$, one finds that $E_x^{(m)'} = 4\pi \sum q_\alpha \int_0^x \check{n}_\alpha^{(m)} dx$ applies. It follows that Eq. (20) for the predicted future field reduces to

$$E_x^{(m+1)} = \frac{4\pi \sum q_\alpha [\int_0^x \check{n}_\alpha^{(m)} dx - \mathbf{J}_{\alpha x}^{(m)} \Delta t]}{(1 + \omega_{p0}^2 \Delta t^2)}, \tag{45}$$

in agreement with Eq. (4) of Ref. [3]. We can see that Eq. (45) includes a corrective term to eliminate density deviations by considering the limit $\omega_{p0} \Delta t \gg 1$ with [illegible]. In response to an electron density excess $\delta\check{n}$ at the edge of a plasma, Eq. (45) will produce the predicted field $E_x = (\delta n/n)(m_e/e)(\Delta x/\Delta t^2)$. By Eq. (19) this will yield a predicted current $j_x^{(m+1)} = -(e/m_e) nE$, and by the continuity, Eq. (40), a corrective change in density for the next cycle $n^{(m+1)} - n^{(m)} = j_x(\Delta t/\Delta x) = -\delta\check{n}$.

The field corrections derived from the density deviations $\delta\check{n}_\alpha^{(m)}$ can also be associated [56] with longitudinal current deviations, i.e.,

$$\delta\mathbf{E}_l^{(m)} = -\nabla\delta\phi^{(m)} = -4\pi\sum q_\alpha\delta\check{\mathbf{j}}_{\alpha l}^{(m)}\,\Delta t^{(m-1)} \equiv -4\pi\sum q_\alpha(\check{\mathbf{j}}_{\alpha l}^{(m)} - \mathbf{j}_{\alpha l}^{(m)})\,\Delta t^{(m-1)}. \tag{46}$$

The $\delta\check{\mathbf{j}}_{\alpha l}$ represent the true excess longitudinal flux over the $\mathbf{j}_\alpha$ predictions of the previous cycle which acted to bring about the density deviations $\delta\check{n}_\alpha$. The longitudinal fluxes can be derived from the full fluxes by the operations: $-\nabla^2\psi = \nabla\cdot\mathbf{j}$ followed by a Poisson solve, and then $\mathbf{j}_l = -\nabla\psi$.

Experience has shown [3, 9, 10, 13, 59] that use of the longitudinal correction provides physically plausible, quasineutral solutions across steep density gradients in the modeling of dense one-dimensional plasmas. In two-dimensional applications, however, use of this correction can have *disastrous* consequences. When the gradients in density are such that $\omega_{p0}^2\,\Delta t^2$ ranges from, say, 1 to 10^2 over a few cells, the addition of the $\nabla\delta\phi$ term leads to the establishment of electrostatic potentials up to 10 times the energy of the hottest electrons produced in laser-driven problems and to the development of B-fields 10 times larger than those determined via an uncorrected calculation. Examples are discusses in Section 10.

At first, we were surprised by these difficulties stemming from the longitudinal E-field correction, since it mimics the Boris [30] correction which has been used successfully in explicit two-dimensional codes since 1970. Furthermore, earlier two-dimensional implicit studies [16–19] had reported no related problems. Later, we found that the new problems arose chiefly in steep density situations that had not been probed before, but which were now accessible, by virtue of the hybrid fluid modeling of the background laser illuminated plasma. More specifically, the new difficulties were related transverse E-field errors introduced along with the longitudinal correction under implicit modeling.

If $\mathbf{j}_z$ is treated explicitly, $[(*) = (m)]$ in Eq. (4), then the addition of $-\nabla\delta\phi^{(m)}$ to $\mathbf{E}^{(m)}$ will produce only a longitudinal change in $\mathbf{E}^{(m+1)}$. But once we go to the Eq. (20) implicit formalism, the effect of this addition is to produce a net change

$$\delta\mathbf{E}^{(m+1)} = -\frac{\nabla\delta\phi^{(m)}}{(1+\omega_{p0}^2\,\Delta t^2)} \tag{47}$$

in the predicted E-field. This change is likely to have a transverse component $\delta\mathbf{E}_t^{(m+1)}$ (for which $\nabla\cdot\delta\mathbf{E}_t^{(m+1)} = 0$), since, generally, $\nabla\times[-\nabla\delta\phi^{(m)}/(1+\omega_{p0}^2\,\Delta t^2)] \neq 0$. The rotational component $\delta\mathbf{E}_t^{(m+1)}$ is negligible when $\omega_{p0}^2\,\Delta t$ is either small compared to unity or nearly constant—the regime of most earlier 2D simulations [16, 18]. This component can produce a change $\delta\mathbf{B}^{(m+1)} = -c\,\Delta t\,\nabla\times\delta\mathbf{E}_t^{(m+1)}$ in the B-field calculated for the next cycle. It can also contribute to the irrotational fields (and potentials) calculated in the next and any subsequent cycles, since in Eq. (20) $\nabla\cdot[\delta\mathbf{E}_t^{(m)}/(1+\omega_{p0}^2\,\Delta t^2)]$ is unlikely to be zero. It can, therefore, lead to the secular growth of $\mathbf{B}$ and ϕ seen in our steep gradient simulations.

B. The Transverse E-field Correction

To eliminate these difficulties stemming from the longitudinal correction, we can employ the Eq. (44) replacement, but with the addition of a transverse field correction as well, i.e., one can use [60, 26]

$$\mathbf{E}^{(m)} \to \mathbf{E}^{(m)''} \equiv \mathbf{E}^{(m)} - \nabla\delta\phi^{(m)} + \nabla \times \lambda^{(m)} \tag{48}$$

in Eqs. (4) and (20). Taking the divergence of Eq. (4) with this alteration, one can see that the additional $\nabla \times \lambda^{(m)}$ term makes no change in the previously achieved agreement between Eqs. (41a) and (41b). The λ-function should be chosen so as to cancel exactly the transverse consequences stemming from the introduction of $-\nabla\delta\phi$. That is, we choose to require that the net correction make no change in the calculated B-field for the next cycle. From Eq. (20) we see that this is accomplished, if

$$\nabla \times \left[\frac{-\nabla\delta\phi^{(m)} + \nabla \times \lambda^{(m)}}{(1 + \omega_{p0}^2\, \Delta t^2)} \right] = 0. \tag{49}$$

For the planar plasma flows modeled, only a z-component is required for λ. Consequently, after multiplication by $c^2\, \Delta t^2$ Eq. (49) rearranges to

$$\frac{\partial}{\partial x}\left(\Lambda_y^2 \frac{\partial \lambda_z^{(m)}}{\partial x} \right) + \frac{\partial}{\partial y}\left(\Lambda_x^2 \frac{\partial \lambda_z^{(m)}}{\partial y} \right) = C(x, y) \tag{50a}$$

with

$$C(x, y) \equiv -\frac{\partial}{\partial x}\left(\Lambda_x^2 \frac{\partial \delta\phi^{(m)}}{\partial y} \right) + \frac{\partial}{\partial y}\left(\Lambda_y^2 \frac{\partial \delta\phi^{(m)}}{\partial x} \right). \tag{50b}$$

The factors Λ_β are defined through Eq. (22c) for the left and bottom cell-wall centers. We can readily solve Eq. (50b) for $\lambda_z^{(m)}$, using the ICCG package employed earlier on Eq. (22b) for B_z. The use of $\lambda = \lambda_z \mathbf{e}_z$ in Eq. (48) completes the field corrections.

Note that with globally implicit $\mathbf{v} \times \mathbf{B}$ differencing $\delta\mathbf{E}^{(m+1)}$ becomes a more complicated algebraic function of $\nabla\delta\phi^{(m)}$ than indicated by Eq. (47) (as evident from Eqs. (14)). Still, $\nabla \times \delta\mathbf{E}_t^{(m+1)} = 0$ can be solved for a corrective λ_z. Again, the greater complexity with this differencing leads to a 9-point, nonsymmetric matrix equation, requiring either the ILUCG or Chebycheff solvers.

As in Eq. (46), the λ-function can be associated with a transverse current deviation,

$$\nabla \times \lambda^{(m)} = -4\pi \sum q_\alpha\, \delta\mathbf{j}_{0\alpha t}^{(m)}\, \Delta t \equiv -4\pi \sum q_\alpha (\tilde{\mathbf{j}}_{0\alpha t}^{(m)} - \mathbf{j}_{\alpha t}^{(m)})\, \Delta t^{(m-1)}, \tag{51}$$

where the $\delta\mathbf{j}_{0\alpha t}$ denote the additional transverse fluxes needed to assure that $\mathbf{B}$ undergoes zero change, when the longitudinal correction $\nabla\delta\phi^{(m)}$ is added.

The use of the net Eq. (48) correction gives well-behaved, physically plausible results in the simulation of plasma problems with steep gradients. Quasi-neutrality is achieved where appropriate. The calculated potentials are $O(\kappa T_e)$ and the B-fields evolve smoothly. See Section 10. However, our assumption that $\mathbf{B}$ should be unaffected by our net correction is somewhat arbitrary and principally justified by its apparent success in simulation.

C. True Current Corrections

We need not use the accumulated density deviations to form the longitudinal E-field correction, or the zero-changed B-field condition to estimate an effective transverse current correction. Instead, we can employ the deviations of the true fluxes $\mathbf{j}_\alpha^{(m+1)}$ from the predicted fluxes $\tilde{\mathbf{j}}_\alpha^{(m+1)}$ to form both corrections simultaneously.

True fluid fluxes are readily available and, in fact, used [see Eq. (36a)] to update the various fluid moments. True particle fluxes can be accumulated, as indicated in Section 3A and Ref. [46], by accounting for the detailed passage of particles within and across cells, such that continuity, Eq. (35a), is obeyed with precision. The improved particle accumulation procedure [46, 61] demands roughly 280 lines of FORTRAN coding, while the older bilinear prescription requires about 24 lines. In explicit models the more tedious accumulation also tends to be more noisy [46] (by referencing one boundary for a typical passing particle instead of two [62]). Thus, the bilinear procedure has generally been preferred. However, with implicit fields the excess electrostatic noise tends to be suppressed, and, more importantly, a transverse correction is automatically obtained—with no a priori assumptions as to its effects on $B^{(m+1)}$.

In their original *explicit* application [46] to simulation problems, the true currents were used directly in a leap-frog scheme to advance the E-fields from level-(m) to level-$(m+1)$. There were no corrections or iterations. Corrections were needed in alternate schemes [30, 62] which accumulated current bilinearly. By contrast, the E-fields in our *implicit* calculations are first advanced with predicted currents, so that the true currents must make their contribution either as a correction deferred to the *next* time step, or iteratively in the present time step. Here we shall discuss the deferral procedure. Iterative correction is detailed in the Appendix.

At the end of each cycle, using the newly calculated $\mathbf{E}^{(m+1)}$ and $\mathbf{B}^{(m+1)}$, we evaluate the predicted currents implied by Eq. (4) by forming

$$-4\pi \sum q_\alpha \tilde{\mathbf{j}}_\alpha^{(m+1)} \Delta t^{(m)} = [(\mathbf{E}^{(m+1)} - \mathbf{E}^{(m)}) - c\,\Delta t^{(m)} \nabla \times \mathbf{B}^{(m+1)}] \tag{52}$$

Subtracting this from the true flux accumulations, we establish $-4\pi \sum q_\alpha \delta \tilde{\mathbf{j}}_\alpha^{(m+1)} \Delta t^{(m)}$. Now in the next cycle *old* data is referenced by the index change

$(m+1) \to (m)$. Thus, to repair the $\mathbf{j}_\alpha^{(m+1)}$ of the next cycle, so as to eliminate the error of the previous cycle, we make the correction

$$\mathbf{E}^{(m)} \to \mathbf{E}^{(m)''} \equiv \mathbf{E}^{(m)} - 4\pi \sum q_\alpha \, \delta\mathbf{j}_\alpha^{(m)} \, \Delta t^{(m-1)} \tag{53}$$

in Eqs. (4) and (20).

To check the accuracy of this correction, we take the divergence of Eq. (53), obtaining

$$\begin{aligned} \nabla \cdot \mathbf{E}^{(m)''} &= \nabla \cdot \mathbf{E}^{(m)} - 4\pi \sum q_\alpha \, \nabla \cdot \delta\mathbf{j}_\alpha^{(m)} \, \Delta t^{(m-1)} \\ &= 4\pi \sum q_\alpha n_\alpha^{(m)} + 4\pi \sum q_\alpha (\check{n}_\gamma^{(m)} - n_\alpha^{(m)}) \\ &= 4\pi \sum q_\gamma \check{n}_\gamma^{(m)}, \end{aligned} \tag{54}$$

which agrees with Eq. (42)—proving that Eq. (53) replicates the longitudinal E-field correction. In addition, the remaining part of the $\delta\mathbf{j}_\alpha^{(m)}$ sum provides a transverse correction replacing the λ-function part of Eq. (48), i.e., replacing Eq. (51). We have found that in the simulation of laser irradiated steep-gradient foil problems the Eq. (53) correction, using the true currents, gives smoothly evolving, physically plausible results. The arising potentials are of $O(\kappa T_e)$. The B-fields calculated are very similar to those from the combined longitudinal and λ-function corrections, Eq. (48), except that B_z contours in lower density regions tend to be smoother and less convoluted (see Section 10). So the current correction approach gives reasonable results, avoids the ad hoc assumptions motivating the use of $\nabla \times \lambda^{(m)}$, avoids the Eq. (50a) elliptic solve, and it can be derived as the first step of a convergent iterative procedure. For these reasons this final correction is peferred. However, should one choose to avoid the complex current accumulation procedures demanded by this method, the combined longitudinal and λ-function corrections remain available as a useful, but approximate, alternative.

The significance of the current correction just described becomes more clear, when it is viewed as a deformed final step of an iterative procedure that seeks to

explanation, see the Appendix.

6. A Typical ANTHEM Cycle

A typical calculational cycle begins with a determination of the time step, which is set to respect the smallest Courant limit imposed by the various plasma components (usually that of the hottest electrons). In addition, Δt is allowed to increase by no more than 20% per cycle. Next, in laser problems, we track in laser light and determine the location of the critical surface.

After this, hot electrons are created. If these electrons are treated as particles, they are introduced at the critical surface and given an appropriate distribution of velocities. This is usually a drifting Maxwellian ejected toward the laser and emitted in a 20° cone about the emission direction. If instead the emitted electrons are a true fluid, then they are produced with zero-drift speed and a temperature corresponding to experiment. In each case cold electrons are destroyed at the emission points, so as to conserve charge. Their energy is added to the emitted hot electrons. The fluid moments are corrected to take the hot electron creation into account.

We next compute the matrix coefficients for the elliptic solvers which determine the B_z field. First, the true current correction is added to the old E-field, following Eq. (53). Generally, we employ the explicit magnetic $\mathbf{v} \times \mathbf{B}$ mode, so next the coefficients for Eq. (23) are constructed. We then go to the ICCG solver package, extract the $B_z^{(m+1)}$ solution, and substitute the result into Eq. (21) (with $(*) = (m)$) to establish $E_x^{(m+1)}$ and $E_y^{(m+1)}$. Except in special tests, *no iterative* correction is performed; the true current correction suffices, so the plasma coordinates are advanced once per time step in these fields.

If we should choose to iterate, we must subcycle through the process of calculating the fields and then advancing the plasma from its level-(m) coordinates, improving the fields and then advancing the coordinates again from level-(m), etc. Finally, the true current correction is added at the beginning of the next cycle for further improvement.

Update of the particles and true fluids follows the Section 4 guidelines. The component cell-wall velocities for the Lagrangian part of the true fluid hydrodynamics are calculated. Then, the coordinates of any particles are updated, and the various moments are accumulated. Finally, the advection phase of hydrodynamics is completed for each true fluid component.

The cycle is completed with the generation of printed and graphical output.

7. The Electrostatic Limit

Electrostatic solutions, for which the effects of electromagnetic waves are neglected, can generally provide a useful subspace for simplified test simulations. For the calculation of such electrostatic solutions, one might be tempted simply to set $\mathbf{B}$ to zero in Eqs. (4) and (19), while suppressing Eq. (2). This is acceptable in one-dimension [13], but fails in two, as evidenced by the fact that in steep-gradient laser-driven problems the calculated electrostatic potential ϕ grows to many multiples of κT_e in just a few cycles.

A successful alternative approach is to take the curl of Eq. (20) for the Faraday's law B-field update, while setting c in Eq. (22a) (and in the $\mathbf{v}_z \times \mathbf{B}^{(m)}/c$ term of Eq. (20)) to a very large value—to say, 10^6 times the physical speed of light. This

forces $\nabla \times \mathbf{E}^{(m+1)} \to 0$, producing the irrotational electrostatic solution. Thus, one obtains

$$\nabla \times \left[\frac{\mathbf{E}^{(m)} - 4\pi \sum q_\alpha \mathbf{J}_\alpha^{(m)} \Delta t + c \Delta t \nabla \times \mathbf{B}'}{(1 + \omega_{p0}^2 \Delta t^2)} \right] = 0, \tag{55}$$

which rearranges to

$$B_z'^{(+)} \equiv -c \Delta t \{ \nabla \times \mathbf{E}_0 \}_z \tag{56a}$$

with

$$-\frac{\partial}{\partial x}\left(\Lambda_x^2 \frac{\partial B_z'}{\partial x} \right) - \frac{\partial}{\partial y}\left(\Lambda_x^2 \frac{\partial B_z'}{\partial y} \right) \equiv B_z'^{(+)}. \tag{56b}$$

As in the case of Eqs. (23), this system is readily solved with the ICCG package for B_z'. The substitution of B_z' for $B_z'^{(m+1)}$ in Eq. (20) (with the $\mathbf{v}_\alpha \times \mathbf{B}$ term suppressed) then provides the electrostatic E-field.

One can take the view that for irrotational results, B_z' constitutes a *virtual B-field*, the curl of which is needed to cancel out the rotational component of $\sum q_\alpha \mathbf{j}_y^{(m+1)}$ in Eq. (4). If c is made uniformly large (say, 10^6 times physical c in the $\nabla \times B_z'$ term, as well), the numerical B'-field values will be negligible, while $c \Delta t \nabla \times \mathbf{B}'$ will continue to balance and cancel the rotational component. Thus, in practice, we calculate electrostatic solutions by simply setting c to large values in Eqs. (20). Special coding for electrostatic tests is thereby avoided. A 10^6-fold c increase has been employed to avoid computational round-off errors that might occur at higher multiplications.

Clearly the function $cB' \Delta t$ plays a role very similar to that played by $\lambda^{(m)}$ in Eq. (49). In fact, our experience with B_z' lead to our use of $\lambda^{(m)}$ for a transverse addition to the usual longitudinal field correction. Note, incidentally, that for quasi-neutral electrostatic solutions the simple longitudinal correction of Eq. (44) suffices. The steep-gradient difficulties requiring more subtle corrections are related to the miscalculation of the B-field, an irrelevancy in the electrostatic limit.

8. Alternate Algorithms

A. The Vector Potential Moment Method

Brackbill and Forslund [16, 17] and later Wallace *et al.* [18] (BFW) use vector and scalar potentials in their "moment method" solution for the implicit fields. Generally, therefore, they solve for all the field components rather than just, say, B_z, E_x, and E_y. But also they leave the pressure tensor implicit [16] or extrapolate the current components while retaining implicit dynamical elements of the pressure

tensor [17, 18]. In each case the currents depend on the fields through a differential relation, e.g.,

$$\mathbf{j}_\chi^{(*)} = \mathbf{j}'_\chi - \nabla \cdot [(\mathbf{j}_\chi^{(*)} - \mathbf{j}'_\chi)(\mathbf{j}'_\chi / n'_\chi)] \frac{\Delta t}{2} + \frac{n_\chi \varepsilon_\chi}{2} \frac{[\mathbf{E}^{(*)} + \mathbf{E}^{(*)} \times \boldsymbol{\Omega}_\chi + (\boldsymbol{\Omega}_\chi \cdot \mathbf{E}^{(*)}) \boldsymbol{\Omega}_\chi]}{(1 + \Omega_\chi^2)}, \tag{57}$$

in [17, 18], rather than algebraically, as with Eq. (7). Here, $\mathbf{j}'_\chi$ is the accumulated component flux following particle extrapolation. Consequently, their fluxes *cannot* be expressed solely as local functions of the E-field, nor can they rearrange their results to the equivalent of Eqs. (10) or (14). BFW therefore turn to global iteration [63–65] of the Maxwell-moment equation system. This implies a significantly slower, and possibly less robust solution process that is possible with vectorized elliptic solvers.

As a second major difference from our approach, the BFW procedure recommends only that the electrostatic potential, $\phi^{(m)}$, should be corrected to agree with the true charge accumulated in cells at the end of the previous cycle. This is equivalent to making only the longitudinal E-field correction, Eq. (44), and must be expected to present computations difficulties in steep density gradient regions.

B. The Direct Method

In their "direct method" approach Langdon and Barnes [20], and Hewett and Langdon (66) extrapolate the particles and accumulate a current $\mathscr{J}'$. Then a corrective current $\delta\mathscr{J}$ due to the effects of motion in the electric and magnetic fields is constructed. They determine, as a consequence of the extrapolation procedure inherent in the direct method [15, 20], that the total implicit current for use in Ampere's law is of the form

$$4\pi \sum q_\chi \mathbf{j}_\chi^{(*)} \Delta t = 4\pi \mathscr{J}' \Delta t + \chi \cdot \mathbf{E}^{(m+1)} - c\, \Delta t\, \nabla \times \zeta \cdot \mathbf{E}^{(m+1)}, \tag{58}$$

in which χ and ζ are matrices which strongly couple the field components, since they include the rotational effects of the B-fields on the particle orbits. This approach introduces current dependencies on the spatial derivatives of $\mathbf{E}$ through the ζ term, so again solution via simple elliptic solvers is unavailable.

Combining Eqs. (58) and (4), one obtains

$$\mathbf{E}^{(m+1)} = \mathbf{E}^{(m)} - 4\pi \mathscr{J}' \Delta t - \chi \cdot \mathbf{E}^{(m+1)} + c\, \Delta t\, \nabla \times [\mathbf{B}^{(m+1)} + \zeta \cdot \mathbf{E}^{(m+1)}]. \tag{59}$$

Langdon and Barnes [20] noted that the divergence of Eq. (59) (which is equivalent to Eq. (41)) implies predicted densities $n_\chi^{(m+1)}$ that can differ from the

true densities $\check{n}_x^{(m+1)}$ achieved when the plasma coordinates are advanced. To correct this error, they considered making the longitudinal correction of Eq. (44), except that instead of adding $-\nabla\delta\phi^{(m)}$ to $\mathbf{E}^{(m)}$ they would add the equivalent, $\nabla\delta\phi^{(m)}/4\pi\,\Delta t$, to $\mathscr{J}'$.

In addition, Langdon and Barnes considered an alternate, purely longitudinal correction to the *advanced E*-field. That is, they suggested the change

$$\mathbf{E}^{(m+1)} \to \mathbf{E}'^{(m+1)} - \nabla\psi, \tag{60}$$

which converts Eq. (59) to

$$\mathbf{E}'^{(m+1)} = \mathbf{E}^{(m)} + (1+\chi)\cdot\nabla\psi - 4\pi\mathscr{J}'\,\Delta t - \chi\cdot\mathbf{E}'^{(m+1)} + c\,\Delta t\,\nabla\times[\cdots]. \tag{61}$$

To correct the density errors they then required that ψ satisfy

$$\nabla\cdot(1+\chi)\cdot\nabla\psi = -\nabla^2\,\delta\phi^{(m)} \equiv 4\pi\sum q_x\check{n}_x^{(m)} - \nabla\cdot\mathbf{E}^{(m)}, \tag{62}$$

in lieu of using Eqs. (43) and (44). Hewett and Langdon (66) subsequently reported that the earlier longitudinal correction lead to difficulties in steep gradient regions and implied corrective currents in the *vacuum*. Since these difficulties were eliminated with the newer Eq. (62) implicit correction, it was recommended.

Equation (62) can be solved directly for ψ by means of elliptic solvers [34, 35, 37, 38]. But a solution can also be obtained by starting with

$$(1+\chi)\cdot\nabla\psi = -\nabla\,\delta\phi^{(m)} + \nabla\times\lambda, \tag{63}$$

since $\nabla\times\lambda$ is invisible to the divergence operator in Eq. (62). Then,

$$\nabla\psi = [1+\chi]^{-1}\cdot(-\nabla\,\delta\phi^{(m)} + \nabla\times\lambda). \tag{64}$$

An equation for λ is obtained by requiring that $\nabla\psi$ is, indeed, irrotational, i.e.,

$$\nabla\times\{[1+\chi]^{-1}\cdot(-\nabla\,\delta\phi^{(m)} + \nabla\times\lambda)\} = 0. \tag{65}$$

For explicit magnetic differencing $\chi = \omega_{p0}^2\,\Delta t^2\mathbf{I}$ with $\mathbf{I}$ the identity diagonal matrix. Thus, Eq. (64) reduces to Eq. (49). With our alternate global implicit differencing the matrix includes a rotation due to the *B*-field [20, 67] leading to a more complex, but solvable equation for a single component $\lambda = \lambda(x, y)\,\mathbf{e}_z$. Once λ has been obtained, Eq. (64) gives $\nabla\psi$ for Eq. (60).

It is, therefore, clear that the direct implicit longitudinal correction is equivalent to our λ-function correction. Both corrections remove charge separation errors under the arbitrary constraint that no *B*-field changes are directly produced as a by-product. This constraint can be avoided by using the Section 5 current corrections

9. HYBRID MODELING

Classical hybrid particle simulation models [63–66] treat the ions as particles and the electrons as a single fluid, lacking all or part [70] of its inertia. These models determine the electron density from the ion data through the quasi-neutral assumption, $n_e \simeq Zn_i$, or the related Gauss's law

$$n_e = Zn_i - \frac{1}{4\pi e}\nabla \cdot \mathbf{E}, \tag{66}$$

so no detailed treatment of the electron dynamics is demanded, except, perhaps, for a concomitant update of an electron energy equation. The classical hybrid schemes have run into difficulties in the modeling of plasmas with neighboring vacuum regions [71], since their implementation relies on the field expressions (when resistivity is low)

$$\mathbf{E} = -\frac{\mathbf{v}_e \times \mathbf{B}}{c} - \frac{1}{en_e}\nabla P_e \tag{67a}$$

with

$$\mathbf{v}_e = \frac{Zn_i\mathbf{v}_i}{n_e} - \frac{c\nabla \times \mathbf{B}}{4\pi e n_e}, \tag{67b}$$

which are singular as $n_e \to 0$. The invocation of an "ad hoc" density floor can suffice in one dimension to allow good calculations for the plasma body, but in the low density surroundings and for two-dimensional plasmas in vacua the results are unreliable.

The single electron fluid in the classical hybrid models corresponds best to the *auxiliary* fluid in our implicit hybrid scheme, since it is used chiefly to compute the fields. Thus, Eq. (67a) goes over to Eq. (20) of our implicit scheme. In conjunction with the auxiliary fluid equation of the moment method, we retain the full Maxwell displacement term, so a "1" appears in concert with $\omega_{p0}^2 \Delta t^2$ (in place of n_e) in the denominator of Eq. (20), and the singularity is removed. Also, the full set of electron inertial terms is retained. Moreover, instead of determining the velocities inferentially, as with Eq. (67b), we update them directly with the aid of either Eq. (7) or (19). Our velocities remain, therefore, finite and well behaved in low density regions.

Our use of an implicit E-field guarantees that the numerical instabilities related to plasma waves are suppressed, allowing $\Delta t \gg \omega_{p0}^{-1}$, as in the classical hybrid models. However, the simple differencing used for the inertial terms in the auxiliary equations of the moment method in *no* way guarantees *positivity* of the densities predicted along with the field solution. For this reason we have chosen to retain the additional true electron fluid, differenced in a spatially stable manner—according to donor-cell or Van Leer—to ensure positivity and long term stability. Alternatively,

one might attempt to include diffusive spatial differencing directly in the auxiliary equations, as recently suggested in a direct method, FCT framework by Denavit [14]. This would lead to iteration of the resultant auxiliary-direct equations for more precise fields, in lieu of the iterative corrections described in the Appendix.

Our present use of an explicit scalar pressure in both the auxiliary and true fluids acts to limit our hybrid time step to an electron Courant value, rather than to the ion Courant value enjoyed by the classical hybrid models. We speculate that the use of an implicit scalar pressure in *both* fluids should permit an increase of the implicit time step up to a value based on the electron drift speed, rather than one based on its thermal speed. For those instances when the electrons track the ions, this should result in a substantial permitted increase in Δt, to values equivalent to the classical hybrid limit. Accordingly, motion of the true fluid can be calculated by established implicit hydrodynamic techniques [72]—with the electrons updated in implicit fields calculated approximately with implicit pressures but simple spatial differencing. This is philosophically different than reaching for an increased time step by way of extrapolation [17, 20], since extrapolation essentially moves material in consistency with the *old* pressure gradients, while the use of implicit scalar pressures moves matter in anticipation of the advanced gradients. Significant motion of the electron fluid through E-fields that can seriously change its dynamics is, therefore, controlled self-consistently in the proposed approach—but not so with extrapolation. The field equations will be more difficult to solve with implicit pressures, but an iteration of the Section 3 procedures, using $P_e^{(m+1)} \simeq n_e^{(m+1)} \kappa T_e^{(m)}$ and Eq. (66), may prove to be workable and sufficient in two dimensions, as it has in more limited one-dimensional investigations [3]. Note that if the true fluid were represented as particles (in such a large -Δt full-particle scheme) the corresponding procedure would demand subcycling of the particles along their orbits [73, 74, 3] to assure an adequate sampling of the self-consistent fields.

10. Demonstrative Calculations

Here we present results from a set of laser illumination runs, performed with ANTHEM for the purpose of demonstrating the relative merits of explicit magnetic differencing compared to globally implicit $\mathbf{v} \times \mathbf{B}$ differencing and the comparative virtues of the various field correction procedures discussed. Related demonstration runs in which classical collisions are active are available in Ref. [26].

Our test runs were performed with the default parameters described in Sections 3 and 4, except as otherwise indicated. Thus, the E-field is fully forward differenced, and $\mathbf{v}^{(*)} \times \mathbf{B}^{(m)}$ is centered implicitly in the velocity and current updates. However, in the elliptic equations for B_z we allow the magnetic force term to be explicit for most of these tests. The runs are all very short, typically requiring 65 cycles performed in 2 min of CRAY-XMP time. Energy is conserved to better than 5% in the course of these runs; conservation will improve when time centering of the implicit

terms in the code is more complete, as suggested in Section 3a. In each case the field is computed without iteration; there is a single advance of each fluid and/or particle component each time step.

Figures 2 to 7 show results for the CO_2 10.6 μm illumination of fully ionized ($Z = 2.6$) slabs of CH_2 plastic. The light enters from the right and runs parallel to the x axis along the grid lines until it reaches the critical surface at $10^{19}\,\mathrm{cm}^{-3}$ electron density. We deposit 27% of an applied intensity of $3 \times 10^{14}\,\mathrm{W/cm}^2$ in the cell just below critical by assumed resonance absorption. The spot is 80 μm in diameter and at the center of a 1000 μm slab. The background electron and ion temperatures are initially set at 100 eV. The laser generated hot electrons are initially emitted at 20 keV, but hydrodynamic expansion of the hot electron fluid rapidly cools these electrons to 10 keV temperatures. We use a 50 by 50 mesh with $\Delta x = \Delta y = 20$ μm. The time step is variable, but typically $\Delta t = 0.12$ ps. At the critical density the plasma frequency $\omega_p = 1.8 \times 10^{14}\,\mathrm{s}^{-1}$ and therefore $\omega_p^2 \Delta t^2 = 431$. The slab is initialized with an exponential-ramp density profile dropping from $1.3 \times 10^{23}\,\mathrm{cm}^{-3}$ electron density down to of $10^{17}\,\mathrm{cm}^{-3}$, which is taken as the floor density n_{vac}. Fluid velocities are set to zero in regions for which $n < n_{\mathrm{vac}}$. Generally, we show the calculated plasma configuration after 5.4 ps of plasma evolution, representing 50 cycles of computation and about 2 min of CRAY-XMP time.

Figure 2 gives results obtained with explicit magnetic differencing and use of the true current correction. Frame (a) displays two-dimensional hot electron density contours which can be calibrated by reference to the one-dimensional density profiles given below in frame (d). These profiles are recorded along a line at $y = 500$ μm. The single fiducial line in frames (a) and (b) represents the calculated deposition point for laser energy. The double fiducials mark the end of the slab at n_{vac}. Clearly, hot electrons have propagated more than 300 μm during the illumination period.

Frame (b) shows the self-consistent B-field generated by thermo-electric influences [39, 40, 75]. Frame (e) taken at the $y = 400$ μm position indicates a near maximum field of 250 kG. Frames (c) and (f) give the electrostatic potential ϕ in contours and profile. There is a small dip in ϕ in the vacuum, and ϕ goes to a maximum of about 20 keV (the initial hot electron temperature) near critical. The additional curve in frame (f) is the containing electric field E_x in relative units. Clearly, the field acts to hold the hot electrons into quasi-neutral agreement with the ions.

Figure 3 gives results achieved when the same system is modeled with the more complex globally implicit $\mathbf{v} \times \mathbf{B}$ differencing. The results are identical in major respects to those of Fig. 2. Minor differences to be noted are slightly broader B-field contours for from the spot, and slight modifications of ϕ in the vacuum and at the outer reaches of the B-field contours. From the essential similarities, we conclude that the simpler explicit magnetic differencing is, in fact, an acceptable procedure.

Figure 4 recalculates the Fig. 2 system with explicit magnetic differencing but *no* longitudinal field correction. The chief deviation from the preceding results is the *leakage* of hot electrons out ahead of the ions into the initial vacuum region.

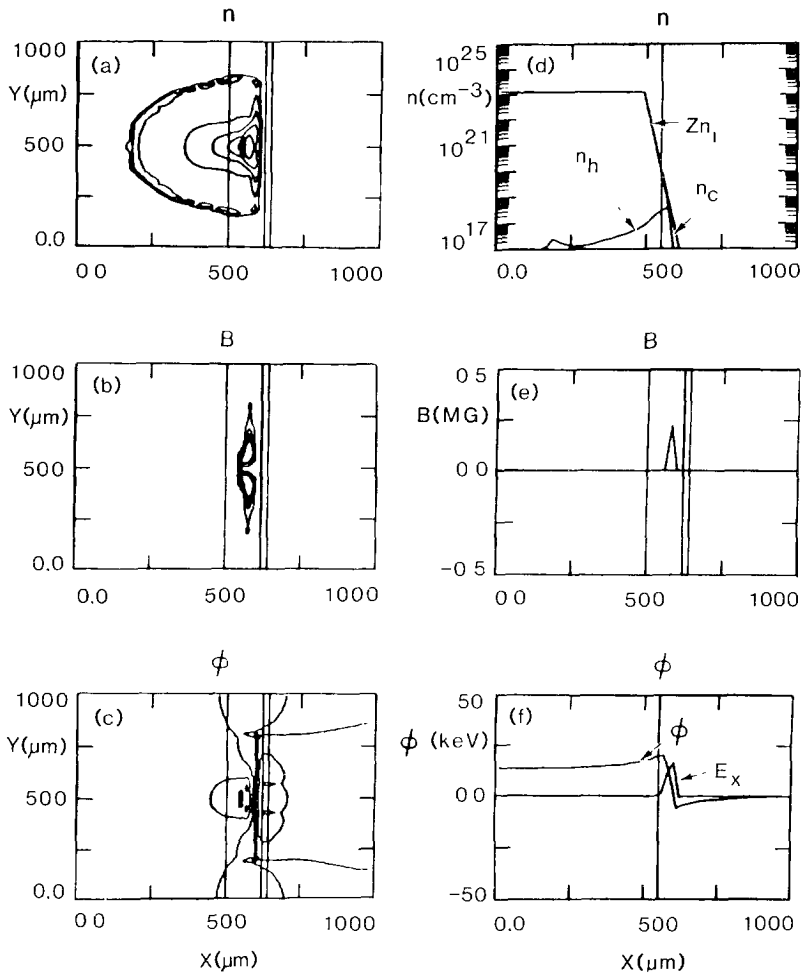

FIG. 2. A test of the utility of explicit magnetic differencing and the true current corrections. Results are for a plastic slab at 5.4 ps under steady illumination by 3×10^{14} W/cm^2 of 10.6 μm light. Details are discussed frame-by-frame in the Section 10 text.

Inspection also shows that the E-field is weaker near the void and further displaced into the void, consistent with the charge separation. Also, the B-field contours are broader, and the up–down, y-directed drop-off of ϕ is more pronounced inside the slab.

Next, Fig. 5 shows the changed results when *just* the longitudinal field correction, Eq. (44), is imposed to halt the charge separation. The hot electron density contours and profile appear to evolve as earlier, but the B-field and potential are markedly different. The B-field is off scale at peak beyond 500 kG, and much more broadly distributed in the vacuum. Relatedly, ϕ achieves a value beyond $3\kappa T_e$ in

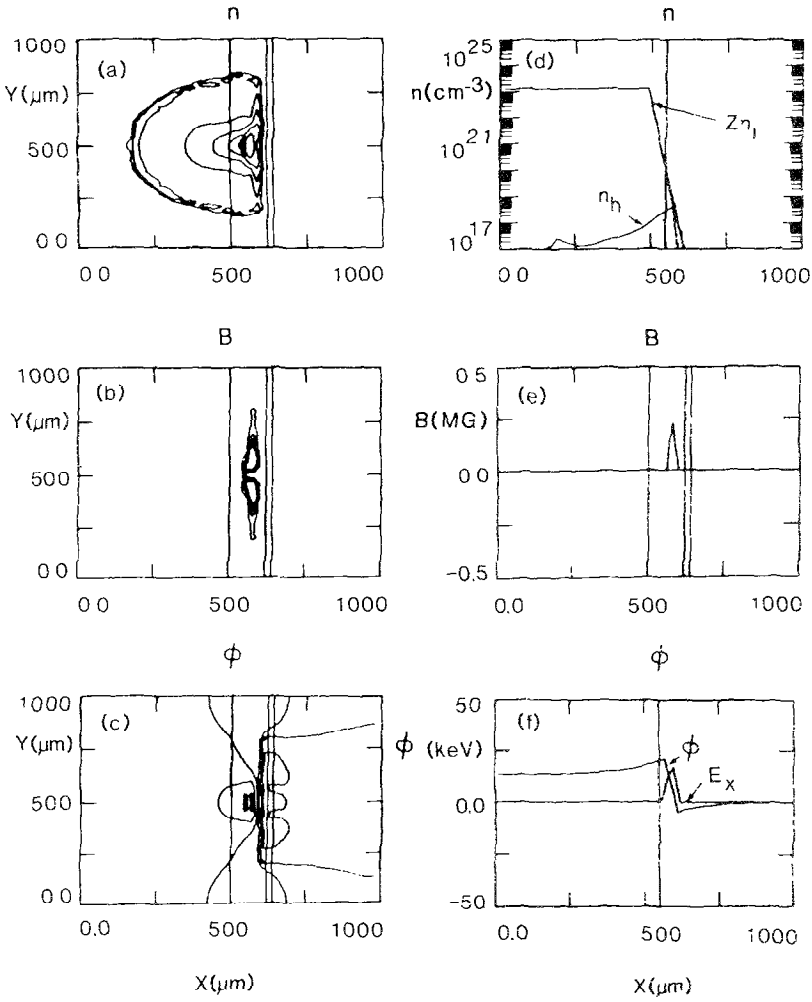

FIG. 3. The same laser and target conditions as for Fig. 2, but with global implicit $\mathbf{v} \times \mathbf{B}$ differencing. The similarity in results testifies to the interchangeability of the two differencing schemes.

front of the laser spot, and reverses sign within the slab. When the same calculation is rerun with Δx, Δy, and Δt all 10 times *smaller* (so that $\omega_p \Delta t$ reduces to about 2) these nonphysical effects disappear, and the results look again like those of Fig. 2 with the true current correction. It was this class of difficulties for large time steps and steep gradients that drove us to develop the $\nabla \times \lambda$ correction and the alternate true current correction.

Figure 6 provides results obtained by using both the longitudinal correction and the λ function. Again, our findings are essentially similar to the results with the true current correction and also with the uncorrected output—except that the charge separation error near the vacuum interface is eliminated. Frame (e) shows a B-field

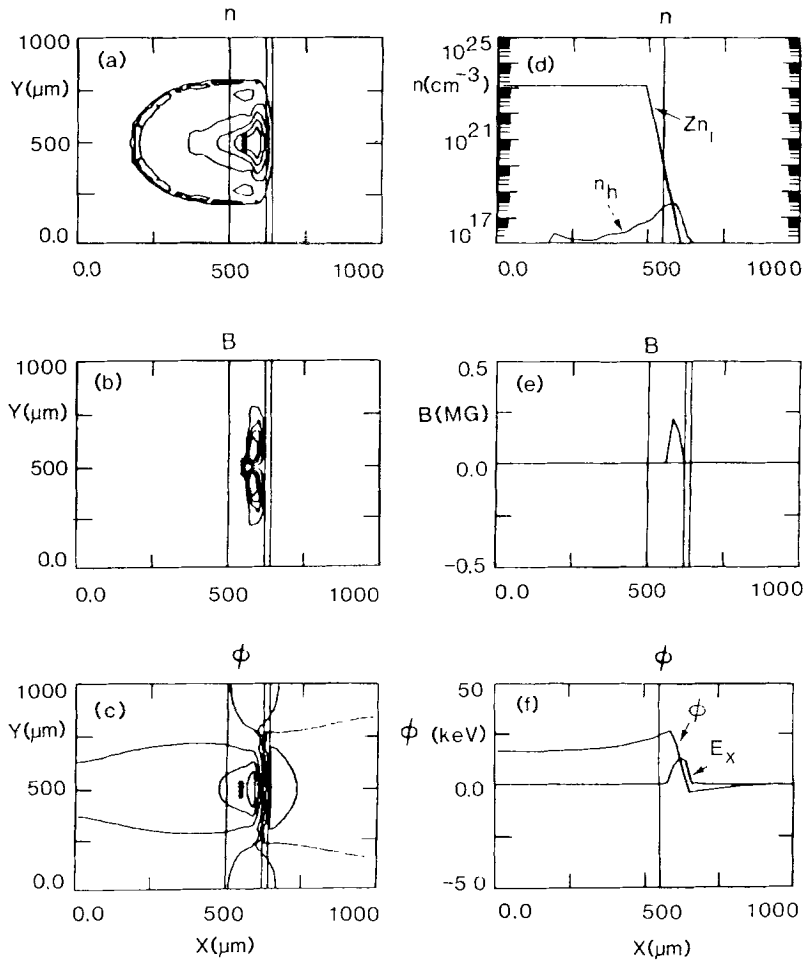

FIG. 4. The Fig. 2 run, but with *no* field correction. Frame (d) shows the hot electrons leaking into the vacuum—in violation of quasi-neutrality.

profile slightly sharper than with the other corrections and potentials closer to the uncorrected potentials inside the slab. The greater simplicity in accumulating currents with the λ function might tend to encourage its use, although the current correction is more fundamental— in its relation to a convergent iterative process for acquiring the exact fields. The Section 8 direct implicit longitudinal correction of Langdon, Barnes, and Hewett [20, 66] should yield results similar to those with the λ function.

Finally, Fig. 7 presents output obtained when the hot electrons are treated as PIC particles, while the background electrons and ions remain fluids. All but fames (d) and (g) are for $t = 5.8$ ps. These and frame (a) show the time development of the hot electron density profiles as well as the positions of the hot electron PIC par-

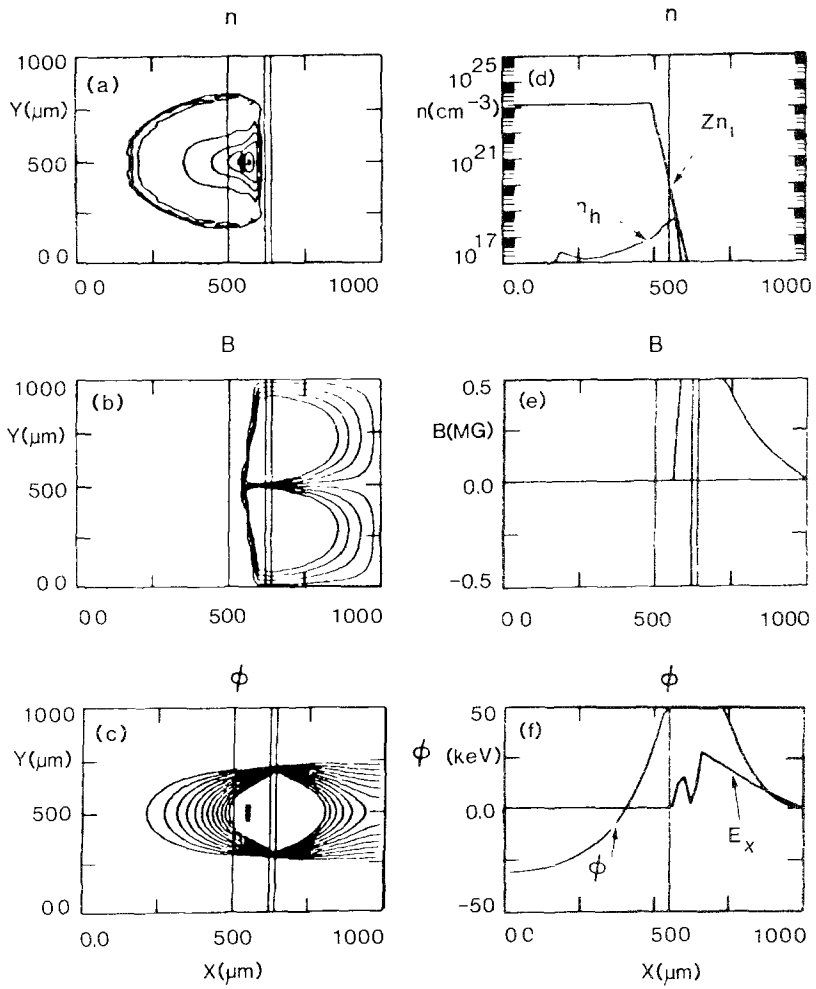

FIG. 5. Nonphysical results for the B-field and ϕ are obtained when just the longitudinal correction is applied to the $\mathbf{E}^{(m)}$-field. B-field excessively fills the vacuum, and ϕ rises to many κT_e. Here, $\omega_p^2 \Delta t^2 > 400$ at critical, so the implicit character of the calculation is strong. The errors vanish for smaller systems, and Δt such that $\omega_p \Delta t < 2$.

ticles. Ten particles are emitted each cycle, so 5000 are present at the end of the run and in frame (a). The particles are produced in a right-drifting maxwellian distribution in a 20° cone about the direction towards the depositing laser. Thus, upon reflection off the sheath neighboring the vacuum, the electrons enter the slab in a more focussed beam than seen in the fluid simulations. The resultant B-field of frames (b) and (e) shows broader contours in the x direction and a weaker intensity at $y = 400$ μm. The ϕ contours are much more irregular, as a consequence of the particle statistics, and the maximum potential is nearly three times the fluidic value,

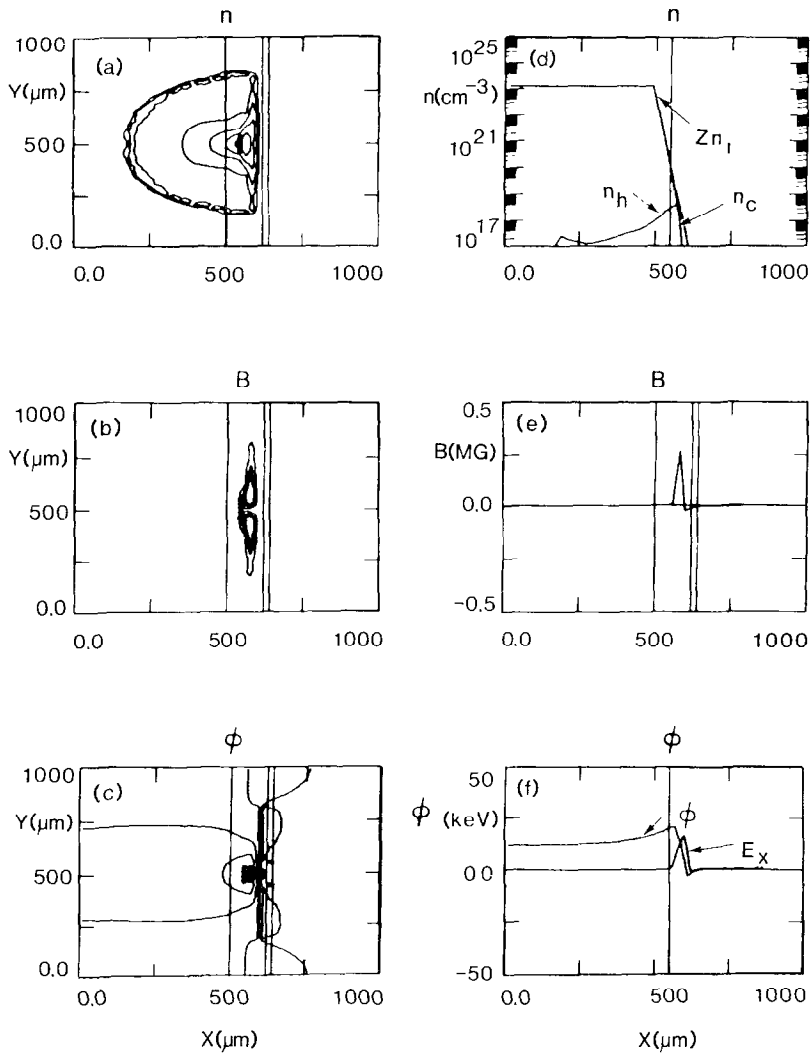

FIG 6. Results obtained using both the longitudinal, $\nabla\,\delta\phi$, correction *and* the $\nabla \times \lambda$ correction. Agreement with the true current correction results of Fig. 2 is good.

since the E-field must be large enough to reflect electrons from the distribution tail at energies exceeding κT_e. Frame (h) gives a u–x phase plot showing particles reflected off the sheath. Here, the solid curve is the mean hot electron velocity. Electrons are specularly reflected off the left boundary. Last, frame (i) shows a smoothed profile of the hot electron density, along with the cold n_c and ion n_i density profiles. The essential point here is that the explicit magnetic differencing and true current corrections are proven effective in hybrid particle simulation.

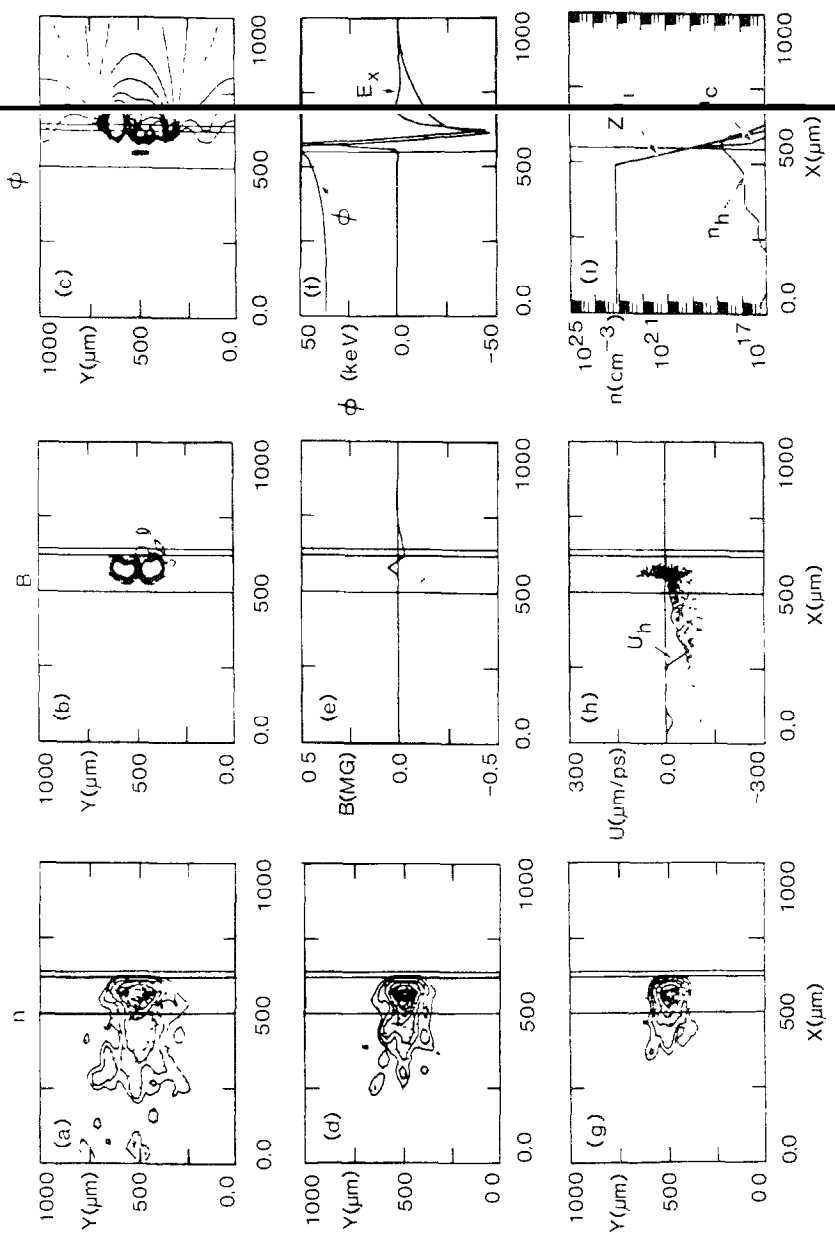

FIG. 7. Results from the use of PIC-particle hot electrons with explicit magnetic differencing and the true current correction. General agreement with the earlier fluid calculations is apparent.

11. Conclusions

We have described a robust and simple two-dimensional algorithm, in part embodied in the ANTHEM code, for the implicit simulation of plasmas. It compares favorably with earlier approaches in terms of facility, efficiency, and applicability to problems manifesting steep density gradients. The implicit field approach can be used with either the particle or fluid modeling of the plasma components, so that widespread full-particle and hybrid applications should be possible.

Appendix A: $\delta\tilde{\mathbf{j}}_\alpha^{(m+1)}$ Iterations

This development expands on the convergence analysis of Ref. [3, Section II.B.4], which, in turn, was derived from the related treatment by Langdon *et al.* [15]. Due to differences between the true and predicted currents, one will generally find that, indeed, following the plasma advance

$$^{(s)}\mathbf{E}^{(m+1)} \neq {}^{(s)}\mathbf{E}^{(m)} - 4\pi \sum q_\alpha {}^{(s)}\tilde{\mathbf{j}}_\alpha^{(m+1)} + c\,\Delta t\,\nabla \times {}^{(s)}\mathbf{B}^{(m+1)}. \tag{A1}$$

That is, equality will prevail using the predicted currents (as required by the Eq. (4) solution), but not using the true currents. Consequently, we seek to iterate the entire system of fields and plasma, such that in the next $(s+1)$ iterate, equality with the true currents is more closely achieved. We, therefore, seek to establish

$$^{(s+1)}\mathbf{E}^{(m+1)} = \mathbf{E}^{(m)} - 4\pi \sum q_\alpha {}^{(s+1)}\tilde{\mathbf{j}}_\alpha^{(m+1)} + c\,\Delta t\ \nabla \times {}^{(s+1)}\mathbf{B}^{(m+1)}. \tag{A2}$$

To make this improvement, we define iterative variations

$$^{(s+1)}\mathscr{D}\mathbf{E}^{(m+1)} \equiv {}^{(s+1)}\mathbf{E}^{(m+1)} - {}^{(s)}\mathbf{E}^{(m+1)}, \tag{A3a}$$

$$^{(s+1)}\mathscr{D}\mathbf{B}^{(m+1)} \equiv {}^{(s+1)}\mathbf{B}^{(m+1)} - {}^{(s)}\mathbf{B}^{(m+1)}, \tag{A3b}$$

$$^{(s+1)}\mathscr{D}\mathbf{j}_\alpha^{(m+1)} \equiv {}^{(s+1)}\mathbf{j}_\alpha^{(m+1)} - {}^{(s)}\mathbf{j}_\alpha^{(m+1)} \tag{A3c}$$

and

$$^{(s+1)}\mathscr{D}\tilde{\mathbf{j}}_\alpha^{(m+1)} \equiv {}^{(s+1)}\tilde{\mathbf{j}}_\alpha^{(m+1)} - {}^{(s)}\tilde{\mathbf{j}}_\alpha^{(m+1)}. \tag{A3d}$$

Then, from Eqs. (19) for iteration level-$(s+1)$ we derive

$$^{(s+1)}\mathscr{D}\tilde{\mathbf{j}}_\alpha \simeq {}^{(s+1)}\mathscr{D}\mathbf{j}_\alpha = \frac{n_\alpha^{(m)} q_\alpha}{m_\alpha}\,\Delta t^{(s+1)}\,\mathscr{D}E \tag{A4a}$$

under the condition that the pressures and $\mathbf{v} \times \mathbf{B}$ terms are evaluated at time level-(m). From the summation of these component equations we construct

$$4\pi \sum q_\alpha {}^{(s+1)}\mathscr{D}\tilde{\mathbf{j}} \simeq \omega_{p0}^2\,\Delta t^{2\,(s+1)}\mathscr{D}\mathbf{E}. \tag{A4b}$$

The approximate equal signs remind us that variations of the true fluxes are only approximately give by the variations of the predicted fluxes, as determined from the moment equations.

These expressions permit us to convert Eq. (A2) to

$$^{(s)}R \equiv -4\pi \sum q_\alpha\, {}^{(s)}\tilde{\mathbf{j}}_\alpha^{(m+1)}\, \Delta t - [({}^{(s)}\mathbf{E}^{(m+1)} - \mathbf{E}^{(m)}) - c\, \Delta t\, \nabla \times {}^{(s)}\mathbf{B}^{(m+1)}] \tag{A5a}$$

$$= -4\pi \sum q_\alpha\, {}^{(s)}\delta\tilde{\mathbf{j}}_\alpha^{(m+1)}\, \Delta t \tag{A5b}$$

$$\simeq (1 + \omega_{p0}^2\, \Delta t^2)\, {}^{(s+1)}\mathcal{Q}\mathbf{E}^{(m+1)} - c\, \Delta t \times {}^{(s+1)}\mathcal{Q}\mathbf{B}^{(m+1)}. \tag{A5c}$$

Here, $^{(s)}R$ is the error residual at iteration level-(s), $^{(s)}\delta\tilde{\mathbf{j}}_\alpha^{(m+1)} \equiv {}^{(s)}\tilde{\mathbf{j}}_\alpha^{(m+1)} - {}^{(s)}\hat{\mathbf{j}}_\alpha^{(m+1)}$ represents the difference between true fluxes and the predicted fluxes, and $4\pi \sum q_\alpha\, {}^{(s)}\hat{\mathbf{j}}_\alpha^{(m+1)}$ is given by Eq. (52). Equation (A5) can be solved for the E-field variations, yielding

$${}^{(s+1)}\mathcal{Q}\mathbf{E}^{(m+1)} \simeq \frac{-4\pi \sum q_\alpha\, {}^{(s)}\delta\tilde{\mathbf{j}}_\alpha^{(m+1)}\, \Delta t^{(m)} + c\, \Delta t\, \nabla \times {}^{(s+1)}\mathcal{Q}\mathbf{B}^{(m+1)}}{(1 + \omega_{p0}^2\, \Delta t^2)}. \tag{A6}$$

Faraday's law, Eq. (2), relates the B- and E-field variations, giving $\mathcal{Q}\mathbf{B} = -c\, \Delta t\, \nabla \times \mathcal{Q}\mathbf{E}$. We use this to eliminate $\mathcal{Q}\mathbf{E}$ after taking the curl of Eq. (A6). Then, to determine the $^{(s+1)}\mathcal{Q}B_z^{(m+1)}$ variations corresponding to the latest $^{(s)}\delta\tilde{\mathbf{j}}_\alpha^{(m+1)}$ values, we solve

$${}^{(s+1)}\mathcal{Q}B_z^{(m+1)} - \frac{\partial}{\partial x}\left(\Lambda_y^2 \frac{\partial\, {}^{(s+1)}\mathcal{Q}B_z^{(m+1)}}{\partial x}\right) - \frac{\partial}{\partial y}\left(\Lambda_x^2 \frac{\partial\, {}^{(s+1)}\mathcal{Q}B_z^{(m+1)}}{\partial y}\right) = {}^{(s)}\mathcal{Q}B_z^{(\tau)} \tag{A7a}$$

with

$${}^{(s)}\mathcal{Q}B_z^{(\tau)} \equiv \left\{ -c\, \Delta t\, \nabla \times \left[\frac{-4\pi \sum q_\alpha\, {}^{(s)}\delta\tilde{\mathbf{j}}_\alpha^{(m+1)}\, \Delta t^{(m)}}{(1 + \omega_{p0}^2\, \Delta t^2)} \right] \right\}_z. \tag{A7b}$$

As earlier, the Λ_β^2 factors in Eq. (A7a) are computed from Eq. (22c) and based on the wall averaged densities n_x and n_y.

The solution for $^{(s+1)}\mathcal{Q}B^{(m+1)}$ is, again, readily supplied by our ICCG solver [34, 35]. With this obtained, Eq. (A6) renders $^{(s+1)}\mathcal{Q}\mathbf{E}^{(m+1)}$. We can, therefore, proceed to construct

$${}^{(s+1)}\mathbf{E}^{(m+1)} = {}^{(s)}\mathbf{E}^{(m+1)} + {}^{(s+1)}\mathcal{Q}\mathbf{E}^{(m+1)} \tag{A8a}$$

and

$${}^{(s+1)}\mathbf{B}^{(m+1)} = {}^{(s)}\mathbf{B}^{(m+1)} + {}^{(s+1)}\mathcal{Q}\mathbf{B}^{(m+1)}. \tag{A8b}$$

Finally, we advance the plasma coordinates in these new fields from their time

level-(m) determinations to *improved* time level-($m+1$) values, ${}^{(s+1)}\mathbf{x}_l^{(m+1)}$ and ${}^{(s+1)}\mathbf{u}_l^{(m+1)}$, while accumulating ${}^{(s+1)}n_\alpha^{(m+1)}$ and ${}^{(s+1)}\tilde{\mathbf{j}}_\alpha^{(m+1)}$—to complete the iterative cycle. This overall procedure can, of course, be repeated in pursuit of still greater improvement.

Comparing Eqs. (53) to Eq. (A6), we observe that with the true current correction procedure we essentially defer calculation of the effects of the current deviations until the next cycle. By skipping the iterative sequence, we avoid costly ICCG solutions for ${}^{(s+1)}\mathscr{D}B_z^{(m+1)}$ and multiple updates of the plasma coordinates each time step. Simulation results with this simplification have, in practice, proven acceptable.

Similarly, comparing Eqs. (49) and (A7b) we see that the λ-function correction, indeed, corresponds to very special transverse current deviations, such that no B-field variations are induced.

To check the convergence of these iterations we can examine the ratio of successive residuals. From Eqs. (A5b) and (52) one can determine that

$$ {}^{(s+1)}R = {}^{(s)}R - 4\pi \sum q_x [{}^{(s+1)}\mathscr{D}\tilde{\mathbf{j}}_x^{(m+1)} - {}^{(s+1)}\mathscr{D}\mathbf{j}_x^{(m+1)}]\,\Delta t. \tag{A9} $$

This can be rearranged to

$$ \frac{{}^{(s+1)}R}{{}^{(s)}R} \simeq \frac{(\omega_{p0}^2\,\Delta t^2)\,{}^{(s+1)}\mathscr{D}\mathbf{E}^{(m+1)} - 4\pi \sum q_x\,{}^{(s+1)}\mathscr{D}\tilde{\mathbf{j}}_x^{(m+1)}\,\Delta t}{(1+\omega_{p0}^2\,\Delta t^2)\,{}^{(s+1)}\mathscr{D}\mathbf{E}^{(m+1)} + c^2\,\Delta t^2\,\nabla\times\nabla\times{}^{(s+1)}\mathscr{D}\mathbf{E}^{(m+1)}}, \tag{A10} $$

by using Eq. (A5c) for ${}^{(s)}R$, and the differential of Eq. (52) to express $4\pi \sum {}^{(s+1)}\mathscr{D}\mathbf{j}_x^{(m+1)}\,\Delta t$ in terms of ${}^{(s+1)}\mathscr{D}\mathbf{E}^{(s+1)}$ and ${}^{(s+1)}\mathscr{D}\mathbf{B}^{(m+1)}$, and by using the differential of Faraday's law to eliminate $\mathscr{D}\mathbf{B}^{(m+1)}$ from ${}^{(s)}R$.

Then for fields with a sample spatial dependence of e^{ikx} the denominator of Eq. (A10) is $(1+\omega_{p0}^2\,\Delta t^2 + k^2c^2\,\Delta t^2)\,\mathscr{D}\mathbf{E}^{(m+1)}$. Clearly, the next residual, ${}^{(s+1)}R$, is zero, if, in fact, equality applies in Eq. (A4b). Also, convergence is faster for shorter wavelength (larger k) disturbances. That is, if the true current's dependence on $\mathscr{D}\mathbf{E}$ is the same as the dependence of the auxiliary fluid current, then the iterative corrections will give the exact field and plasma solution after a single pass (at level $s=1$). Generally, this will not be the case. For example, while the auxiliary fluids will obey Eq. (49a), the x component of any true hybrid fluid elements is given by Eqs. (36a) and (36b). Only in the pure second-order case ($\eta=0$)—with negligible Lagrangian phase density changes—are the densities contributing to the true and auxiliary currents the same. Similarly, any particles crossing a cell-wall boundary, and contributing to the currents there, will experience the E-field from the four nearest cell-wall centers, while (for $\mathbf{B}=0$) the auxiliary fluid currents sense only a local cell-wall centered field. Complexities of the field-to-particle area weighting and the particle-to-current accumulation procedures go further to guarantee some inequality in Eq. (A4b). Reference [3] discusses such details in a one-dimensional context. Borrowing from these one-dimensional results, we can conclude that in spatially near-uniform systems convergence will be faster, since the relatively larger

stencil for the particle-felt fields and Van Leer hydrodynamics will matter less. Again, experience has shown that simple deferral of a single iterative correction to the next cycle—the true current procedure—is sufficient for acceptable simulation results.

ACKNOWLEDGMENTS

The author is grateful to J. Brackbill, C. Cranfill, D. Forslund, M. Jones, T. Jordan, J. Kindel, K. Lee, T. Manteuffel, and J. Wallace at Los Alamos, to D Besnard at Limeil, to D. Hewett and B. Langdon at Livermore, to D. Nicholas and R. Evans at the Rutherford, to P. Velarde at the Technical University of Madrid, and to M. Haines, A. Bell, and G. Richard at Imperial College for helpful discussions during the course of this work. The work benefitted from attendance by the author at CECAM workshops in Orsay and summer tenure as a Visiting Fellow at Imperial College

REFERENCES

1. R L. MORSE, in *Methods of Computational Physics, Vol.* 9, edited by B. Alder, B. Fernbach, and M. Rotenberg (Academic Press, New York, 1970), p.213
2. A. B LANGDON AND B. F. LASINSKI, in *Methods in Computational Physics, Vol.* 16, edited by J Killeen (Academic Press, New York, 1976), p. 327.
3. R. J MASON, in *Multiple Time Scales*, edited by J. U. Brackbill and B I. Cohen (Academic Press, New York, 1985), p. 233.
4. A B. LANGDON, *J. Comput. Phys.* **30**, 202 (1979)
5. R J. MASON, in *Laser Interactions and Related Plasma Phenomena, Vol.* 5 (Proceedings, Fifth Workshop on Laser Interactions with Matter, Rochester, NY, Nov. 5–9, 1979), edited by H J Schwarz and H. Hora (Plenum, New York, 1981), p. 743.
6. R J. MASON, in *Proceedings of the Informal Conference on Particle Codes for Fusion, Napa CA, Dec.* 10, 1979, *U. C Berkeley*, Electronics Research Laboratory Report UCB/ERL M79/79, Paper 23, 1979 (unpublished).
7. R J. MASON, *Phys. Fluids* **23**, 2204 (1980)
8. R J MASON, *Bull. Amer. Phys. Soc.* **25**, No. 2, 926 (1980)
9. R J MASON, *J. Comput. Phys.* **41**, 233 (1981)
10. R. J. MASON, *J Comput Phys.* **51**, 484 (1983).
11. T. L. CRYSTAL, J DENAVIT, AND C. E. RATHMANN, *Comments Plasma Phys. Controlled Fusion* **5**, 17 (1979).
12. J. DENAVIT AND J. M. WALSH, Paper PC3, 9th Conference on the Numerical Simulation of Plasmas, Northwestern University, June 1980.
13. J DENAVIT, *J. Comput Phys.* **42**, 33 (1981).
14. J. DENAVIT, *Space Plasma Simulations*, edited by M Ashour-Abdalla and D. A. Dutton (Reidel, Dordrecht, 1900), p. 85.
15. A. FRIEDMAN, A. B. LANGDON, AND B. I. COHEN, *Comments Plasma Phys Controlled Fusion* **6** 225 (1981); A B Langdon, B. I. Cohen, and A Friedman, *J. Comput. Phys.* **51**, 107 (1983).
16. J U BRACKBILL AND D. W FORSLUND, *J Comput. Phys.* **46**, 271 (1982).
17. J. U. BRACKBILL AND D. W FORSLUND, in *Multiple Time Scales*, edited by J. U Brackbill and B. I. Cohen (Academic Press, New York, 1985), p 271.
18. J M. WALLACE, J U BRACKBILL, AND D. W FORSLUND, *J Comput. Phys.* **63**, 434 (1986).
19. D. C. BARNES, T KAMIMURA, J.-N. LEBOEUF, AND T TAJIMA, *J. Comput. Phys.* **52**, 484 (1983); T KAMIMURA, T. TAJIMA, J.-N. LEBOEUF, AND D. C BARNES, *Bull. Amer. Phys Soc.* **27**, 1035 (1982).

20. A. B. LANGDON AND D. C. BARNES, in *Multiple Time Scales*, edited by J. U. Brackbill and B. I. Cohen, (Academic Press, New York, 1985), p. 335.
21. K. B. QUEST, D. W. FORSLUND, J. U BRACKBILL, AND K. LEE, *Geophys. Lett.* **10**, 471 (1983).
22. D. W. FORSLUND, K. B QUEST, J. U. BRACKBILL, AND K LEE, *J. Geophys. Res.* **89**, 2142 (1984)
23. J. U. BRACKBILL, D. W. FORSLUND, K. B. QUEST, AND D. WINSKE, *Phys. Fluids* **27**, 2682 (1984)
24. D. WINSKE, M. TANAKA, C. S. WU, AND K. B. QUEST, *J. Geophys. Res.* **90**, 123 (1985).
25. R. J. MASON, "Hydrodynamic Aspects of 2D Laser Generated Transport," The Rezoner Workshop. Asilomar, CA, June 19–22, 1983; Los Alamos Report, LA-10112-c, p. 61, 1984 (unpublished).
26. R. J MASON AND C. W. CRANFILL, *IEEE Trans. Plasma Sci.* **PS-14**, 45 (1986).
27. D. BESNARD AND R J MASON, Limeil Report CEA-N-2413, 1984 (unpublished).
28. B. VAN LEER, *J. Comput. Phys.* **23**, 276 (1972); **32**, 101 (1979).
29. B. GODFREY, *J. Comput. Phys.* **15**, 504 (1974).
30. J P. BORIS, in *Proceedings, 4th Conference on the Numerical Simulation of Plasmas, Naval Research Laboratory, Nov.* 2–3, 1970, edited by J. P. Boris and R. A Shanny, (Office of Naval Research of the Navy, 1970), p. 3.
31. S. I. BRAGINSKII, *Rev. Plasma Phys.* **1**, 205 (1965).
32. J. VON NEUMAN AND R. D RICHTMEYER, *J. Appl Phys.* **21**, 232 (1950).
33. A SHESTAKOV AND D. V ANDERSON, *Comput. Phys Commun.* **30**, 31 (1983).
34. T. JORDAN, in *Elliptic Problem Solvers II*, (Academic Press, New York, 1985), p 127.
35. Available from T Jordan or T. Manteuffel, C-division, Los Alamos, (1985).
36. R. A. GENTRY, R. E. MARTIN, AND B. J. DALY, *J. Comput. Phys.* **1**, 87 (1966).
37 J. A. MEIJERINK AND H. A. VAN DER VORST, *Math. Comput.* **31**, 148 (1977)
38. D. KERSHAW, *J. Comput. Phys.* **26**, 43 (1978).
39. J. A. STAMPER, E A. MCCLEAN, AND B RIPIN, *Phys Rev. Lett.* **40**, 1177 (1978).
40. R J. MASON, *Phys. Rev. Lett.* **42**, 239 (1979)
41. R. J. MASON, *Phys. Fluids* **15**, 1082 (1972).
42. R. J. MASON AND J. M. WALLACE, *Bull. Amer. Phys. Soc* **30**, 1547 (1985)
43. R J. MASON, J. M WALLACE, AND K. LEE, Los Alamos LA-UR-86-1977; in *Proceedings, Sixth International Topical Conference on High-Power Electron and Ion-Beam Research and Technology, Kobe, Japan June* 9–12, 1986, p 295.
44. J. M WALLACE, J. U. BRACKBILL, C. W CRANFILL, D. W. FORSLUND, AND R. J MASON, Los Alamos Report LA-UR-86-1064; *Phys. Fluids*, in press.
45. J. M. WALLACE, X-1, Los Alamos, private communication, March 1986.
46. R. L. MORSE AND C. W. NIELSON, *Phys. Fluids* **14**, 830 (1971)
47. G R. GISLER AND M. E JONES, 11th International Conference on Numerical Simulation of Plasmas, Montreal, Canada, June 25–27, 1985; Los Alamos Report LA-UR-85-124, 1985 (unpublished).
48. M. E JONES AND G. R. GISLER, 11th International Conference on Numerical Simulation of Plasmas, Montreal, Canada, June 25–27, 1985; Los Alamos Report LA-UR-85-118, 1985 (unpublished).
49. R. B. DEBAR, Lawrence Livermore Laboratory Report UCID-19683, 1974 (unpublished).
50. W. G. SUTCLIFFE, Lawrence Livermore Laboratory Report UCID-17013, 1974 (unpublished).
51. D. L. YOUNGS, in *Numerical Methods for Fluid Dynamics*, edited by K W. Morton and M. J. Baines (Academic Press, New York, 1982), p 273.
52. D L. BOOK, J. P. BORIS, AND K. HAIN, *J Comput. Phys.* **18**, 248 (1975).
53. C. W. HIRT AND B. D. NICHOLS, *J. Comput. Phys.* **39**, 201 (1981).
54. P. LOTSTEDT, *J. Comput. Phys.* **47**, 211 (1982).
55. R L. CARMAN, D. W FORSLUND, AND J. M. KINDEL, *Phys. Rev. Lett.* **46**, 29 (1981).
56. J. D JACKSON, *Classical Electrodynamics* (Wiley, New York, 1975), p. 221.
57. Available from J. Adams, P. Swartzrauber, and R. Sweet, National Center for Atmospheric Research, Boulder, Colorado 80307, 1982.
58. R SWEET, *SIAM J. Numer. Anal.* **14**, 706 (1977).
59. R. J. MASON, *Phys. Rev. Lett.* **47**, 652 (1981).
60. The λ-function was first discussed by R. J. Mason at the 14th Annual Anomalous Absorption

Conference, Charlottesville, Va., May 6–11, 1984; R J MASON, M. HAINES, AND R. EVANS, *Bull Amer. Phys. Soc.* **29**, 1382 (1984).
61. Available from M. Jones and G. Gisler, Los Alamos, 1985.
62. A. B. LANGDON, *Phys. Fluids* **15**, 1149 (1972).
63. P A. BERNHARDT AND J. U. BRACKBILL, *J. Comput. Phys.* **53**, 382 (1984).
64. P CONCUS AND G. H. GOLUB, *SIAM J. Numer Anal.* **10**, 1103 (1973).
65 C W. NIELSON AND H. R. LEWIS, *Methods Comput. Phys.* **16**, 367 (1976)
66 D W. HEWETT AND A. B. LANGDON, Lawrence Livermore Laboratory Report UCRL-94591; *J. Comput. Phys*, in press.
67 C. K BIRDSALL AND A. B. LANGDON, *Plasma Physics via Computer Simulation* (McGraw-Hill, New York, 1985), p. 341.
68. R J. MASON, *Bull. Amer. Phys. Soc* **14**, No. 2, 1043 (1969); R. J. MASON, *Phys. Fluids* **14**, 1943 (1971)
69. D W FORSLUND AND J. P. FREIDBERG, *Phys Rev. Lett.* **27**, 1189 (1971).
70 R J. MASON, *Phys Fluids* **15**, 845 (1972); J. A. BYERS, B. I. COHEN, W. C. CONDIT, AND J D. HANSON, *J Comput. Phys.* **27**, 363 (1978), D. W HEWETT AND C. W NIELSON, *J. Comput. Phys.* **29**, 219 (1978); D. W. HEWETT, *J. Comput Phys.* **38**, 378 (1980); D S. HARNED, *J. Comput. Phys.* **47**, 452 (1982)
71. A. G. SGRO AND C W NIELSON, *Phys Fluids* **19**, 126 (1976).
72 F H. HARLOW AND A A. AMSDEN, *J. Comput. Phys.* **8**, 197 (1971).
73. J.-C ADAM, A. GOURDIN-SERVENIERE, AND A. B LANGDON, *J. Comput. Phys* **47**, 229 (1982).
74. B I. COHEN, in *Multiple Time Scales*, edited by J. U. Brackbill and B. I. Cohen (Academic Press, New York, 1985), p 311
75 D W FORSLUND AND J. U. BRACKBILL, *Phys. Rev. Lett.* **48**, 1614 (1982)